



저작자표시-비영리-변경금지 2.0 대한민국

이용자는 아래의 조건을 따르는 경우에 한하여 자유롭게

- 이 저작물을 복제, 배포, 전송, 전시, 공연 및 방송할 수 있습니다.

다음과 같은 조건을 따라야 합니다:



저작자표시. 귀하는 원저작자를 표시하여야 합니다.



비영리. 귀하는 이 저작물을 영리 목적으로 이용할 수 없습니다.



변경금지. 귀하는 이 저작물을 개작, 변형 또는 가공할 수 없습니다.

- 귀하는, 이 저작물의 재이용이나 배포의 경우, 이 저작물에 적용된 이용허락조건을 명확하게 나타내어야 합니다.
- 저작권자로부터 별도의 허가를 받으면 이러한 조건들은 적용되지 않습니다.

저작권법에 따른 이용자의 권리는 위의 내용에 의하여 영향을 받지 않습니다.

이것은 [이용허락규약\(Legal Code\)](#)을 이해하기 쉽게 요약한 것입니다.

[Disclaimer](#)

Master's Thesis

Vacancy-driven Na Superionic Conduction
in New Ca-doped Na_3PS_4
for All-Solid-State Na-ion Batteries

Chang Ki Moon

Department of Energy Engineering
(Battery Science and Technology)

Graduate School of UNIST

2018

Vacancy-driven Na Superionic Conduction
in New Ca-doped Na₃PS₄
for All-Solid-State Na-ion Batteries

Chang Ki Moon

Department of Energy Engineering
(Battery Science and Technology)

Graduate School of UNIST

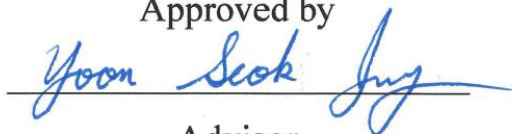
Vacancy-driven Na Superionic Conduction
in New Ca-doped Na_3PS_4
for All-Solid-State Na-ion Batteries

A thesis
submitted to the Graduate School of UNIST
in partial fulfillment of the
requirements for the degree of
Master of Science

Chang Ki Moon

01. 08. 2018

Approved by



Advisor


Yoon Seok Jung

Vacancy-driven Na Superionic Conduction
in New Ca-doped Na₃PS₄
for All-Solid-State Na-ion Batteries

Chang Ki Moon

This certifies that the thesis of Chang Ki Moon is approved.

01. 08. 2018

signature

Advisor: Yoon Seok Jung

signature

Young Sik Kim

signature

Jun Hee Lee

Abstract

As the applications of lithium-ion batteries (LIBs) are expanding from mobile electronic devices to electrical vehicles (EVs) and energy storage systems (ESSs), concerns about their safety hazard also increased.¹ The safety issues for LIBs are originated from flammable organic liquid electrolytes.² In this regard, all-solid-state lithium-ion batteries (ASLBs) employing nonflammable inorganic solid electrolytes (SEs) have emerged as a promising alternative.³⁻⁷ In another aspect, as the price of Li sources soared, Na-ion batteries (NIBs) are considered to be promising next-generation batteries especially for ESS application.⁸ Due to similarities of NIBs to LIBs in terms of chemistry/electrochemistry, extensive research efforts have been focused on NIBs in recent years.⁹ Furthermore, development of Na-ion conducting SEs opened a research field for all-solid-state Na-ion batteries (ASNBs).¹⁰⁻¹⁵

Herein, the highly conductive Ca-doped Na_3PS_4 SEs and their use for bulk-type ASNBs will be presented in this thesis.

Contents

Abstract	4
List of Figures	8
List of Tables	10
Nomenclature	12
I. Introduction	13
II. Theoretical & Mathematical Development	15
2.1 Principle of Lithium-ion Batteries	15
2.2 All-Solid-State Sodium-ion Batteries	17
2.2.1 Inorganic and organic solid electrolytes	19
III. Experimental Method & Materials	20
3.1 Preparation of Materials	20
3.2 Materials Characterization	20
3.3 Computational details	20
3.4 Electrochemical Characterization	21
IV. Results & Discussion	22
V. Conclusion	36
VI. Supporting information	37
6.1 Conductivity from ^{23}Na NMR results	37

6.2 Formation energy from DFT	38
6.3 Supporting figures	39
6.4 Supporting tables	47
References	58

List of Figures

Figure 1. Schematic diagram of conventional lithium-ion batteries

Figure 2. Schematic diagram of bulk-type all-solid-state batteries³

Figure 3. Characterization of Ca-doped Na_3PS_4 ($\text{Na}_{3-2x}\text{Ca}_x\text{PS}_4$ ($0 \leq x \leq 0.300$)) prepared at 700 °C. a) Powder XRD patterns for $\text{Na}_{3-2x}\text{Ca}_x\text{PS}_4$. b) X-ray Rietveld refinement profile for $\text{Na}_{2.730}\text{Ca}_{0.135}\text{PS}_4$. c) Crystal structure of $\text{Na}_{2.730}\text{Ca}_{0.135}\text{PS}_4$ with the unit cell outlined. d) Calculated formation energy as a function of c/a ratio, varied by Ca doping and V_{Na} concentration. The filled, empty, and half-filled symbols are denoted to represent vacancy positions and concentrations in Na1 or Na2 site of $t\text{-Na}_3\text{PS}_4$. The circles denote $\text{Na}_{2.9375}\text{PS}_4$ (empty or filled in black) and $\text{Na}_{2.8750}\text{PS}_4$ (half-filled in green). The other symbols represent concentrations of vacancy, and positions of Ca and V_{Na} for Ca-doped Na_3PS_4 ; $\text{Na}_{2.750}\text{Ca}_{0.125}\text{PS}_4$ (up and down triangle in red). $\text{Na}_{2.625}\text{Ca}_{0.125}\text{PS}_4$ (square in blue and diamond in violet, empty or filled). The short dashed line (---) and the dash dot line (-·-·-) indicate the c/a ratios for $t\text{-Na}_3\text{PS}_4$ by the experiment¹⁶ and calculation, respectively. e) Na-ion conductivities at 25 °C and activation energies for $\text{Na}_{3-2x}\text{Ca}_x\text{PS}_4$. Nyquist plots are shown in the inset in (e).

Figure 4. Results of ^{23}Na static NMR for $t\text{-Na}_3\text{PS}_4$ and Ca-doped cubic Na_3PS_4 ($\text{Na}_{2.730}\text{Ca}_{0.135}\text{PS}_4$). a) ^{23}Na NMR spectra and b) ^{23}Na NMR spin-lattice relaxation rate $1/T_1$ at different temperatures. Activation energies are shown in (b).

Figure 5. Calculated migration barriers for Na vacancy (V_{Na}) in the undoped and Ca-doped Na_3PS_4 . The insets show the initial, transition, and final states. a) Out-of-plane and b) in-plane migration barriers for $\text{Na}_{2.875}\text{PS}_4$. c) Out-of-plane and d) in-plane migration barriers for $\text{Na}_{2.750}\text{Ca}_{0.125}\text{PS}_4$.

Figure 6. MSD depending on the time step for a) 1100 K and b) 700 K.

Figure 7. Electrochemical performance of $\text{TiS}_2/\text{Na-Sn}$ ASNBs using $c\text{-Na}_3\text{PS}_4$ and Ca-doped Na_3PS_4 ($\text{Na}_{2.730}\text{Ca}_{0.135}\text{PS}_4$) at 30 °C. a) First two-cycle discharge-charge voltage profiles at $50 \mu\text{A cm}^{-2}$ (0.06C). b) Charge capacity as a function of cycle number, varied by different current densities. The numbers are the current densities in $\mu\text{A cm}^{-2}$.

Figure S1. Powder XRD patterns for $\text{Na}_{3-2x}\text{Ca}_x\text{PS}_4$ prepared at 700 °C. Unknown peaks are d

enoted ‘*’ .

Figure S2. X-ray Rietveld refinement profiles for $\text{Na}_{3-2x}\text{Ca}_x\text{PS}_4$ prepared at 700 °C.

Figure S3. Arrhenius plots of Na-ion conductivities for $\text{Na}_{3-2x}\text{Ca}_x\text{PS}_4$ prepared at 700 °C.

Figure S4. XRD patterns for $\text{Na}_{3-2x}\text{Ca}_x\text{PS}_4$ prepared at 550 °C.

Figure S5. Conductivities and activation energies at 25 °C for $\text{Na}_{3-2x}\text{Ca}_x\text{PS}_4$ prepared at 700 °C and 550 °C.

Figure S6. Calculated migration barriers for Na vacancy (V_{Na}) in the Na_3PS_4 ($\text{Na}_{2.750}\text{Ca}_{0.125}\text{PS}_4$). The inset shows the initial, transition, and final states. Migration barriers on the plane under the Ca^{2+} ion (a, b) and on the plane containing Ca^{2+} ion (c, d).

Figure S7. MSD depending on the time step for a) 1400 K, b) 800 K, c) 600 K, and d) 500 K.

Figure S8. Discharge-charge voltage profiles for $\text{TiS}_2/\text{Na-Sn}$ ASNBs employing $\text{Na}_{2.730}\text{Ca}_{0.135}\text{PS}_4$.

List of Tables

Table 1. Calculated vacancy formation energy for Na_3PS_4 without and with Ca-doping.

Table 2. Calculated Na vacancy (V_{Na}) energy barriers for Na_3PS_4 without and with Ca-doping.

Table S1. Crystallographic information for $\text{Na}_{3-2x}\text{Ca}_x\text{PS}_4$ prepared at 700 °C, obtained by the Rietveld analysis.

Table S2. Crystallographic data and Rietveld refinement results for the sample with $x = 0.000$ for $\text{Na}_{3-2x}\text{Ca}_x\text{PS}_4$ prepared at 700 °C.

Table S3. Selected interatomic distances and angles for the sample with $x = 0.000$ for $\text{Na}_{3-2x}\text{Ca}_x\text{PS}_4$ prepared at 700 °C.

Table S4. Crystallographic data and Rietveld refinement results for the sample with $x = 0.075$ for $\text{Na}_{3-2x}\text{Ca}_x\text{PS}_4$ prepared at 700 °C.

Table S5. Selected interatomic distances and angles for the sample with $x = 0.075$ for $\text{Na}_{3-2x}\text{Ca}_x\text{PS}_4$ prepared at 700 °C.

Table S6. Crystallographic data and Rietveld refinement results for the sample with $x = 0.120$ for $\text{Na}_{3-2x}\text{Ca}_x\text{PS}_4$ prepared at 700 °C.

Table S7. Selected interatomic distances and angles for the sample with $x = 0.120$ for $\text{Na}_{3-2x}\text{Ca}_x\text{PS}_4$ prepared at 700 °C.

Table S8. Crystallographic data and Rietveld refinement results for the sample with $x = 0.135$ for $\text{Na}_{3-2x}\text{Ca}_x\text{PS}_4$ prepared at 700 °C.

Table S9. Selected interatomic distances and angles for the sample with $x = 0.135$ for $\text{Na}_{3-2x}\text{Ca}_x\text{PS}_4$ prepared at 700 °C.

Table S10. Crystallographic data and Rietveld refinement results for the sample with $x = 0.150$ for $\text{Na}_{3-2x}\text{Ca}_x\text{PS}_4$ prepared at $700\text{ }^\circ\text{C}$.

Table S11. Selected interatomic distances and angles for the sample with $x = 0.150$ for $\text{Na}_{3-2x}\text{Ca}_x\text{PS}_4$ prepared at $700\text{ }^\circ\text{C}$.

Table S12. Crystallographic data and Rietveld refinement results for the sample with $x = 0.180$ for $\text{Na}_{3-2x}\text{Ca}_x\text{PS}_4$ prepared at $700\text{ }^\circ\text{C}$.

Table S13. Selected interatomic distances and angles for the sample with $x = 0.180$ for $\text{Na}_{3-2x}\text{Ca}_x\text{PS}_4$ prepared at $700\text{ }^\circ\text{C}$.

Table S14. Crystallographic data and Rietveld refinement results for the sample with $x = 0.225$ for $\text{Na}_{3-2x}\text{Ca}_x\text{PS}_4$ prepared at $700\text{ }^\circ\text{C}$.

Table S15. Selected interatomic distances and angles for the sample with $x = 0.225$ for $\text{Na}_{3-2x}\text{Ca}_x\text{PS}_4$ prepared at $700\text{ }^\circ\text{C}$.

Table S16. Crystallographic data and Rietveld refinement results for the sample with $x = 0.300$ for $\text{Na}_{3-2x}\text{Ca}_x\text{PS}_4$ prepared at $700\text{ }^\circ\text{C}$.

Table S17. Selected interatomic distances and angles for the sample with $x = 0.300$ for $\text{Na}_{3-2x}\text{Ca}_x\text{PS}_4$ prepared at $700\text{ }^\circ\text{C}$.

Table S18. Characteristics for sulfide Na superionic conductors.

Table S19. Chemical potential of Na and Ca for decomposed products.

Nomenclature

LIBs	Lithium-ion batteries
EVs	Electric vehicles
ESSs	Energy storage systems
ASLBs	All-solid-state lithium-ion batteries
SEs	Solid electrolytes
NIBs	Na-ion batteries
ASNBs	All-solid-state sodium-ion batteries
c-Na ₃ PS ₄	Cubic Na ₃ PS ₄
t-Na ₃ PS ₄	Tetragonal Na ₃ PS ₄
NMR	Nuclear magnetic resonance spectroscopy
PEO	Poly(ethylene oxide)
BASE	B ^γ -alumina solid electrolyte
XRD	X-ray diffraction
DFT	Density-functional theory
PBE	Perdew-Burke-Ernzerhof
GGA	Gradient approximation
PAW	Projector-augmented wave
MP	Monkhorst-pack
BZ	Brillouin zone
NEB	Nudged elastic band method
MD	Molecular dynamics
PEEK	Polyaryletheretherketone
V _{Na}	Na vacancy
bcc	Body-centered cubic
MSD	Mean square distance

I. Introduction

Because of the high energy and power densities of lithium-ion batteries (LIBs), they have become vital components in portable electronic devices. Nowadays, their range of applications is expanded to large-scale areas such as battery-driven electric vehicles (EVs) and energy storage systems (ESSs).¹ However, in case of the conventional LIBs using organic liquid electrolytes, they have some problems like flammability, leakage, low Li-ion transference number and so on.² Furthermore, the cost issues for lithium originated from the limited resources, the recent rapid rises in the price of Li_2CO_3 , and the geologically uneven distribution are serious obstacles for large-scale application.⁸ In this regard, all-solid-state sodium-ion batteries (ASNBs) could be a solution.^{3, 10-15} Sodium is very abundant resources rather than lithium. Moreover, it has similar redox potential (Na: -2.71 V vs. NHE, Li: -3.04 V vs. NHE at 25°C) and chemistry to lithium.⁸ Solid electrolytes (SEs) also have many other merits compared to organic liquid electrolytes such as high thermal stability, high transference number, wide operating temperature etc.¹⁷ Although β -alumina ($\sim 10^{-2}$ S cm^{-1} at room temperature) was the first commercialized Na-ion conductors for Na-S batteries aiming for the application to large-scale energy storage systems,¹⁸ these oxide electrolytes are not suitable to fabricate room-temperature-operable ASNBs because they need a deteriorating high-temperature sintering process.^{3, 10} In contrast, sulfide electrolytes are simply sinterable by cold-pressing owing to their covalent nature of the bonds.^{3, 10, 19} Moreover, recently, sulfide Na superionic conductors (10^{-4} - 10^{-3} S cm^{-1} at room temperature) have been extensively developed.

Tatsumisago and co-workers developed the first sulfide Na superionic conductor, cubic Na_3PS_4 (c- Na_3PS_4), showing a conductivity of 0.2 mS cm^{-1} at room temperature, which was contrasted by a previously known tetragonal Na_3PS_4 (t- Na_3PS_4 , 0.001 mS cm^{-1}).¹⁰ By X-ray structural analysis, the high conductivity of the cubic phase was attributed to existence of the three-dimensional ionic conduction pathways between Na1 and Na2 sites.²⁰ Consistently, the first-principles investigations showed that the occupancy of Na2 site (or Na disorder) be the key to the high ionic conductivity in c- Na_3PS_4 .²¹ Then, extensive efforts for further developments have been followed.

The first approach was an aliovalent substitution of P. The replacement of P in c- Na_3PS_4 with 6 mol.% Si resulted in 0.74 mS cm^{-1} .¹¹ And ~ 0.25 mS cm^{-1} was also achieved by doping with Ge, Ti and Sn in Na_3PS_4 ($\text{Na}_{3+x}\text{M}_x\text{P}_{1-x}\text{S}_4$, M: Ge^{4+} , Ti^{4+} , Sn^{4+}).²² These enhancements were explained that the excess Na, which led to an increased occupancy of the interstitial Na2 site, enabled the increase in conductivity.^{11, 20} This reasoning was supported by the subsequent theoretical calculation results.²¹ The second direction was an isovalent substitution of P or S in Na_3PS_4 with the larger element of Sb, As, Se: High ionic conductivities of ~ 1 mS cm^{-1} were achieved for tetragonal Na_3SbS_4 ,^{13, 23} tetragonal $\text{Na}_3\text{P}_{0.62}\text{As}_{0.38}\text{S}_4$,¹⁵ and cubic Na_3PSe_4 .^{12, 24} The last strategy was to generate Na vacancy defect. Contrary to the attention

to the cubic structure as the origin of high ionic conductivity of c- Na_3PS_4 in the initial report,¹⁰ ab initio calculations showed that a stoichiometric c- Na_3PS_4 is a poor ionic conductor whereas an introduction of Na vacancies drastically enhances the conductivities.^{21, 24-25} Consistently, it was reported that creation of Na vacancy by aliovalent substitution of S in Na_3PS_4 with Cl, which resulted in tetragonal $\text{Na}_{2.9375}\text{PS}_{3.9375}\text{Cl}_{0.0625}$, could achieve a high conductivity of 1 mS cm^{-1} .¹⁴ However, this value was obtained by using spark-plasma-sintered pellets, where grain boundary or inter-particle resistances could be significantly minimized, compared with the pellets prepared by conventional cold-pressing process.

Herein, the development of the new sodium superionic conductor will be presented in this thesis, Ca-doped cubic Na_3PS_4 . Aliovalent substitution of Na in t- Na_3PS_4 with Ca results in the cubic phase ($\text{Na}_{3-2x}\text{Ca}_x\text{PS}_4$) and creates Na vacancies, enabling to drastically enhance the ionic conductivities up to $\sim 1 \text{ mS cm}^{-1}$ at 25°C ($x = 0.135$) by using simple cold-pressing process. The fast ionic movements in Ca-doped c- Na_3PS_4 are investigated by ^{23}Na solid-state nuclear magnetic resonance (NMR) spectroscopy. Density functional theory (DFT) calculations confirm the evolution of cubic structure by Ca-doping, the excellent Ca-dopability, and the increased activation barrier by Ca-doping. Furthermore, promising electrochemical performance of $\text{TiS}_2/\text{Na-Sn}$ ASNBs employing $\text{Na}_{2.730}\text{Ca}_{0.135}\text{PS}_4$ is highlighted.

II. Theoretical & Mathematical Development

2.1 Principle of Lithium-ion Batteries

A battery is the system that chemical energy of the electrode materials is converted to electric energy by using electrochemical reactions. The types are classified into the primary battery and secondary (rechargeable) battery. The primary battery can be used once for a certain period of time. On the other hand, the secondary battery can be used repeatedly for a long time by recharging.²⁶

In the secondary battery, the ion inserted into electrode is a carrier that stores electric energy in electrode by achieving charge neutrality with electrons come from current collectors. The ion can also accelerate the reaction rate within the electrode by moving quickly toward the electrode in the electrolytes areas. Furthermore, the storable amounts of electric energy are determined by the quantity of ions. Therefore, the electrode materials and the type of ion are the main components of deciding the actually storable electric energy. Generally, it is called the lithium secondary batteries using the carriers as lithium-ion.²⁶

The batteries used in mobile devices such as cell-phones, laptops, camcorders, etc. are the lithium secondary batteries. They have the advantages that they have high working potential and can be used repeatedly. In addition, they have high energy density because lithium-ion is a light carrier. Normally, lithium secondary batteries use transition metal oxide materials as cathode and carbon materials as anode. In case of using electrolytes as liquid electrolytes, it is called lithium-ion batteries (LIBs).²⁶ And their schematic diagram is presented in Figure 1.

More specifically, cathode materials should have the stable structure because lithium-ion in the lattice structure participate in reversible redox reactions. Accordingly, transition metal oxide materials are usually used as cathode materials. On the other hand, anode materials should have the standard reduction potential similar to lithium for high energy storage. In case of electrolytes, Li salts and organic liquid electrolytes which have high electrochemical, thermal, chemical stability are used. Furthermore, for preventing short circuit by contact between cathode and anode, the separators composed of polymer materials which can be melted at high temperature or ceramic materials having high thermal stability are used.²⁶

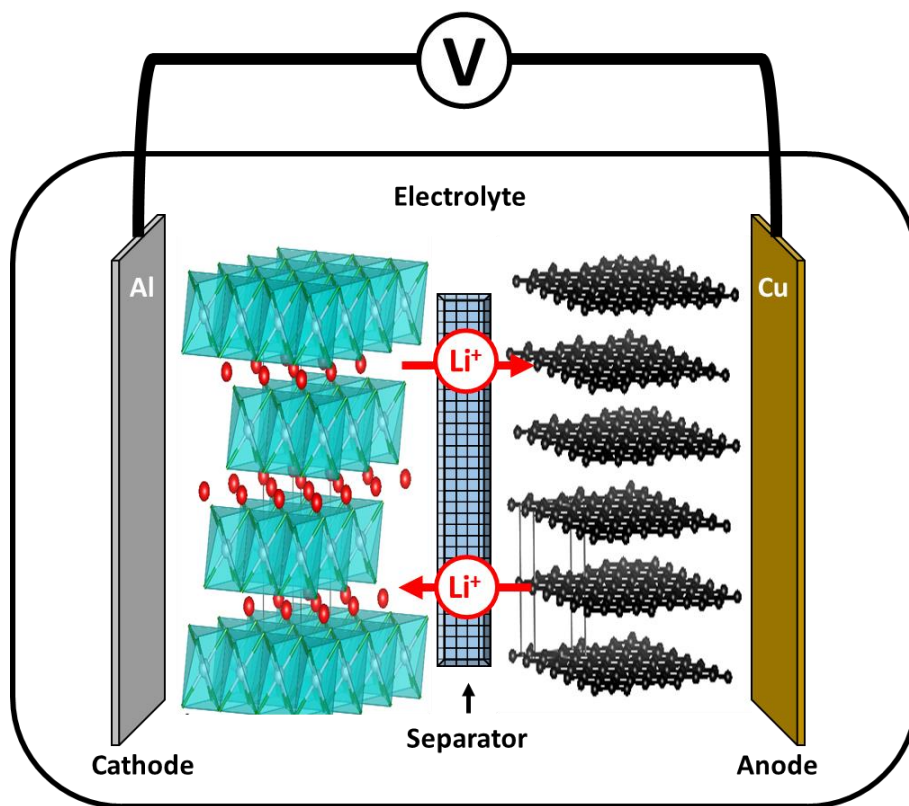


Figure 1. Schematic diagram of conventional LIBs

2.2 All-Solid-State Sodium-ion Batteries

Since the first lithium-ion batteries (LIBs) using organic liquid electrolytes are commercialized in the early 1990s by Sony Corporation,²⁷ LIBs have been widely used for portable electronic devices.¹⁻² However, these conventional LIBs are having difficulties in expanding their application areas to large-scale storage systems. Because the conventional LIBs suffer from their flammability, leakage, low Li-ion transference number, etc.² Furthermore, there exist the cost issues for lithium originated from the limited resources, the recent rapid rises in the price of Li_2CO_3 , and the geologically uneven distribution.⁸ In this regard, all-solid-state sodium-ion batteries (ASNBs) using inorganic solid electrolytes (SEs) are promising alternative to conventional LIBs.^{3, 10-15} Sodium has not only similar redox potential but also chemistry to lithium. Additionally, it is very abundant resources rather than lithium.⁸ Moreover, SEs have several advantages compared to organic liquid electrolytes: broad operating temperature, non-flammability, unity transference number (the cation is only mobile), absence of desolvation.^{3, 17}

In all-solid-state batteries, there are two kinds of fabrication processes. One is the thin film type which uses the expensive vacuum deposition equipment.²⁸⁻²⁹ Therefore, their application areas are restricted to small-scale systems. The other one is the bulk type method. This method doesn't require the highly expensive vacuum deposition process. Hence, this bulk type process is promising for not only portable electronic devices but also large-scale applications. And the schematic diagram of this bulk type all-solid-state batteries are shown in Figure 2.^{3, 30-32}

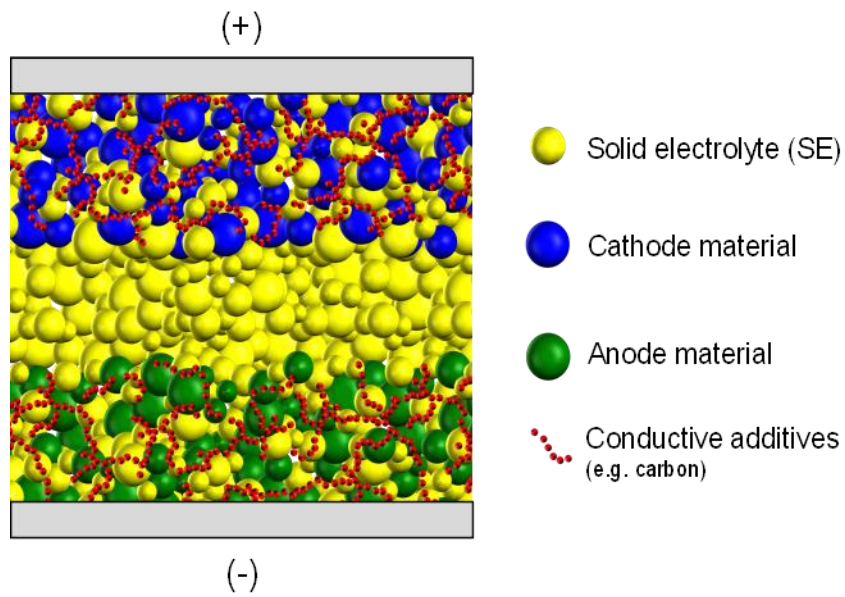


Figure 2. Schematic diagram of bulk-type all-solid-state batteries³

2.2.1 Inorganic and organic solid electrolytes

Although organic liquid electrolytes-based batteries have superior electrochemical performance, they suffer from serious safety issues such as flammability, leakage, undesired concentration polarization and narrow operating temperature. In contrast, the solid electrolytes (SEs) do not have these drawbacks.¹⁷ Thanks to these characteristics, they are considered as a promising candidate for the large-scale energy storage systems.^{3-7, 10-15}

The SEs can be categorized as organic and inorganic. The representative organic solid electrolyte (or solid polymer electrolyte) is poly(ethylene oxide) (PEO). This organic solid electrolyte has several advantages, such as flexibility, light weight, stability with lithium metal, good processability, low shear modulus, high resistance to volume changes of the electrodes in the cell.^{7, 9} However, there are also some disadvantages. The critical drawback is low ionic conductivity at room temperature (10^{-5} ~ 10^{-7} S cm^{-1}).³³ Therefore, most of organic SEs should be operated at relatively high temperature (at least 60°C).³⁴⁻³⁵ In case of inorganic SEs, on the other hand, they have higher ionic conductivity at room temperature and thermal stability compared to organic SEs. From these reasons, many research have been performed.^{7, 9}

More specifically, the inorganic SEs can be divided into three types: oxide, sulfide and the others (hydride, halide, borate or phosphate, etc.).^{3, 7} The sodium β'' -alumina solid electrolyte (BASE, β'' - Al_2O_3),³⁶⁻³⁷ NASICON ($\text{Na}_{1+x}\text{Zr}_2\text{Si}_x\text{P}_{3-x}\text{O}_{12}$, $0 < x < 3$)³⁸⁻³⁹ are the well-known oxide SEs. Their ionic conductivities are 10^{-3} ~ 10^{-4} S cm^{-1} at room temperature. These values are higher than organic SEs. Furthermore, they can be handled in the atmosphere and have high electrochemical stability.⁷ However, it is hard to apply the oxide SEs to bulk-type ASNBs, because of their high interfacial resistance between electrolytes and electrodes.^{32, 40-41} For solving this problem, a sintering process is performed. Unfortunately, after this process, although the interfacial resistance is significantly decreased, unwanted side reactions are occurred.⁴⁰⁻⁴¹ Therefore, the oxide SEs are not suitable for bulk-type ASNBs. In contrast of these oxide SEs, the sulfide SEs are suitable for bulk-type ASNBs because of their deformability.^{10, 32} The bulk-type ASNBs using sulfide SEs are fabricated by simple cold-pressing method.^{10, 32} Therefore, there are no side reactions during the fabricating process. This is the reason why the sulfide SEs are extensively studied.^{3-5, 9-10, 17, 30-31}

III. Experimental Method & Materials

3.1 Preparation of Materials

The t-Na₃PS₄ or Ca-doped Na₃PS₄ powders were prepared by mechanochemical milling of stoichiometric mixture of Na₂S (Sigma Aldrich), CaS (99.9%, Sigma Aldrich), and P₂S₅ (99%, Sigma Aldrich) at 500 rpm for 3-5h, followed by heat-treatment at 700 °C or 550 °C for 12 h in a sealed fused silica ampoule. For the preparation of the c-Na₃PS₄ powders, the same milling condition as for the Ca-doped Na₃PS₄ was employed, followed by heat-treatment at 270 °C for 1 h in a sealed fused silica ampoule.

3.2 Materials Characterization

For the X-ray diffraction (XRD) measurements, the samples were sealed hermetically using Be window inside the glove box. D8-Bruker Advance diffractometer equipped with Cu K α radiation (1.54056 Å) was used with a continuous scanning mode of 0.025° s⁻¹. Rietveld refinements were carried out using the GSAS program. Profiles were fitted with a pseudo-Voigt function. The ²³Na static NMR spectra and the spin-lattice relaxation rate 1/T₁ were acquired by using 400 MHz Avance II+ (Bruker solid-state NMR), for which the ²³Na resonance frequency was 105.84 MHz. Samples were sealed in 4 mm ZrO₂ rotor under Ar-filled glove box. All signals were obtained after $\pi/2$ pulse at temperature range of 165-435 K. Chemical shifts were calibrated to 0.1 M NaCl aqueous solution.

3.3 Computational details

Density-functional theory (DFT) calculations in the Perdew-Burke-Ernzerhof (PBE) generalized gradient approximation (GGA) in the software package VASP and the pseudopotentials generated under projector-augmented wave (PAW) method are used. To find structural ground states, a 4 x 4 x 4 Monkhorst-pack (MP) k-point grid was used for integrations within the Brillouin zone (BZ) based on t-Na₃PS₄ unit cell containing 16 atoms. Energy cut-off for plane wave basis was set to 500 eV and force criteria for the structure optimization was 0.01 eV/Å

Activation barrier for the Na vacancy migration was calculated by the nudged elastic band method (NEB). The supercell contains 8 formula units of t-Na₃PS₄ to minimize the interaction between the periodic cells. A 3 × 3 × 2 k-point grid was used and the plane-wave energy cutoff was set to 500 eV for the NEB calculation.

Gamma-point only used for the molecular dynamics (MD) simulations as a K-points set. About 4.2%

of Na vacancies with and without Ca ions are introduced in the MD simulations (one Na ion is removed from the supercell containing 24 Na ions), to figure out the role of Ca ions. The MD simulations were taken on the canonical ensemble and the time step was set to 0.2 ps. Temperatures were chosen at 1400K, 1100K, 800K, 700K, 600K and 500K, and the MD simulations were performed 40000 time steps for statistical analysis.

3.4 Electrochemical Characterization

After the $\text{Na}_{3-2x}\text{Ca}_x\text{PS}_4$ pellets were prepared by cold-pressing at 370 MPa, the ionic conductivity was measured by an AC impedance method using an Iviumstat (IVIUM Technologies Corp.) with symmetric Na-ion blocking $\text{Ti}/\text{Na}_{3-2x}\text{Ca}_x\text{PS}_4/\text{Ti}$ cells. The $\text{TiS}_2/\text{Na-Sn}$ ASNBs were fabricated as follows: Composite electrodes were prepared from the $\text{TiS}_2/\text{c-Na}_3\text{PS}_4$ or $\text{TiS}_2/\text{Na}_{2.730}\text{Ca}_{0.135}\text{PS}_4$ mixture with a weight ratio of 50:50. Na_3Sn prepared by mixing of Na metal (Sigma Aldrich) with Sn metal powders (Sigma Aldrich) served as the counter electrode, exhibiting an operating voltage of ~ 0 V (vs. Na/Na^+). As the separating solid electrolyte bilayer, 100 mg of c- Na_3PS_4 pellets were used. 10 mg of the as-prepared electrodes were spread on the separating solid electrolyte layer, followed by pressing at 370 MPa. Then, 50 mg of the as-prepared Na_3Sn was attached on the other side of separating solid electrolyte layer by pressing at 370 MPa. All the procedures were performed in a polyaryletheretherketone (PEEK) mould (diameter = 13 mm) with two Ti metal rods as current collectors. All processes for fabricating the all-solid-state cells were performed in an Ar-filled dry box. Galvanostatic charge-discharge measurements were performed at 30 °C between 1.0-2.5 V.

IV. Results & Discussion

Ca^{2+} ion is the most suitable divalent ion that can substitute Na^+ ion because of their similar ionic sizes (Ca^{2+} : 100 pm, Na^+ : 102 pm). Figure 3a shows the X-ray diffraction (XRD) patterns of $\text{Na}_{3-2x}\text{Ca}_x\text{PS}_4$ prepared by solid-state reaction at 700 °C. Without Ca-doping ($x = 0.000$), doublet peaks appear, which is an indicative of tetragonal phase. As the amount of Ca increases, however, the doublet peaks are merged to be the single ones, reflecting evolution of the cubic phase. However, those single peaks are seen to be asymmetric, implying coexistence of the cubic and tetragonal phases, which is confirmed by X-ray Rietveld refinement analysis later. As an unknown phase starts to evolve at $x = 0.450$ (Figure S1), the doping range of Ca in Na_3PS_4 is determined to be $0 < x < 0.450$. Figure 3b presents an X-ray Rietveld refinement profile for $\text{Na}_{2.730}\text{Ca}_{0.135}\text{PS}_4$. All the peaks could be indexed to the cubic structure ($a = 6.9768(1)$ Å, $Z = 2$, $I\bar{4}3m$, Table S1). The Rietveld refinement results for all the compositions are also provided in Figure S2 and Tables S2-17. The refinement was carried out by assuming the co-existence of Ca-free t- Na_3PS_4 and Ca-doped c- Na_3PS_4 phases. The unit cell structure consists of a body-centered cubic sublattice of PS_4^{3-} tetrahedra through which Na1 sites with higher occupancies and Na2 sites with lower occupancies are interconnected in three-dimensional pathways (Figure 3c). Ca occupies in the Na1 site, which agrees well with the DFT calculation. As the amount of Ca is increased, the lattice volume for Ca-doped c- Na_3PS_4 is slightly decreased ($\sim 1\%$ for $\text{Na}_{2.730}\text{Ca}_{0.135}\text{PS}_4$, Table S1), which could be explained by the slightly smaller ionic size of Ca^{2+} than Na^+ .

DFT calculations were carried out to investigate the formation energies and the corresponding c/a ratio, varied by Ca-doping and Na vacancy (V_{Na}) which is generated to compensate the higher charge of Ca^{2+} (Figure 3d). A calculated c/a ratio for the pristine t- Na_3PS_4 is 1.021 which is in good agreement with the experimental observation (1.017).¹⁶ The calculated structures with different vacancy-concentrations ($\text{Na}_{2.9375}\text{PS}_4$ and $\text{Na}_{2.875}\text{PS}_4$) and -sites ($V_{\text{Na}1}$ vs. $V_{\text{Na}2}$) maintain tetragonal geometries with $c/a = 1.017$ -1.031. Therefore, V_{Na} without Ca doping does not induce the cubic structure. In contrast, V_{Na} with Ca doping stabilizes the cubic structure. As shown in the triangles in Figure 3d (the red region of ‘Ca + V_{Na} ’, $\text{Na}_{2.750}\text{Ca}_{0.125}\text{PS}_4$), when Ca and V_{Na} coexist, the c/a ratio tends to decrease to 0.995 and 0.98, exhibiting the most stable energies. Also, when more V_{Na} is added (the blue region of ‘Ca + $2V_{\text{Na}}$ ’, $\text{Na}_{2.625}\text{Ca}_{0.125}\text{PS}_4$, denoted squares and diamonds), the structure gets even closer to cubic geometry. The tetragonal-to-cubic phase transition could be associated with the interaction of Ca^{2+} and V_{Na} . The detailed vacancy formation energies for undoped and Ca-doped Na_3PS_4 are also compared in Table 1. The formation energies for Ca-doped Na_3PS_4 (~ 0.6 eV) are approximately half of those for the undoped Na_3PS_4 (~ 1.0 eV), indicating the excellent dopability of Ca^{2+} with inducing V_{Na} in Na_3PS_4 . In particular, I find that V_{Na} near Ca^{2+} is the most stable. Strong coulombic repulsion between Ca^{2+} and Na^+ ions prevents Na^+ ions from being located in the original Na site close to Ca^{2+} , which creates Na

vacancies around Ca^{2+} .

Variation of the Na-ionic conductivities at 25 °C as a function of Ca substitution (x) in a series of $\text{Na}_{3-2x}\text{Ca}_x\text{PS}_4$, measured by AC impedance method using ion-blocking $\text{Ti}/\text{Na}_{3-2x}\text{Ca}_x\text{PS}_4/\text{Ti}$ symmetric cells, are displayed in Figure 3e (Nyquist plots and Arrhenius plots of conductivities are shown in the inset in Figure 3e, and Figure S3, respectively). $t\text{-Na}_3\text{PS}_4$ without Ca-doping shows a conductivity of 0.077 mS cm^{-1} . This value is lower than that for $c\text{-Na}_3\text{PS}_4$ (0.2^{10} or 0.1 mS cm^{-1} in this work) but much higher than that for $t\text{-Na}_3\text{PS}_4$ in a previous report ($\sim 0.001 \text{ mS cm}^{-1}$).¹⁰ The discrepancy may stem from different Na vacancies, affected by experimental conditions such as impurities.²⁴⁻²⁵ As the amount of Ca-doping (x) increases, the conductivity drastically increases and hits a maximum value of 0.94 mS cm^{-1} at $x = 0.135$, which is comparable to those for other state-of-the-art sulfide Na superionic conductors (Table S18, pros and cons for each materials are also compared). The subsequent increase of the amount of Ca (x) results in the decrease in conductivities (e.g, 0.12 mS cm^{-1} at $x = 0.30$). Despite the enhancement in conductivity by Ca-doping, the activation energies for Ca-doped Na_3PS_4 (0.36-0.49 eV) turned out to be higher than other superionic conductors (typically, 0.2-0.3 eV)³ and, surprisingly, even higher than that for $t\text{-Na}_3\text{PS}_4$ (0.35 eV), which will be discussed in later section. For the samples prepared at 550 °C, the Ca-doping-driven transition from tetragonal to cubic phases and enhancement in conductivities along with the increased activation energies are also confirmed (Figures S4, S5).

The Arrhenius equation for conductivity is given by Equation 1.⁴²

$$\sigma T = A_T \exp(-E_a/k_B T) \quad (1)$$

where σ is the conductivity, T is the temperature in K, A_T is the pre-exponential factor, E_a is the activation energy (or activation barrier), k_B is the Boltzmann constant.

The pre-exponential factor A_T in the Arrhenius equation for ionic conductivity is a function of the site occupancy for mobile ions (n_c), according to Equation 2.⁴²

$$A_T \propto n_c(1-n_c) \quad (2)$$

As demonstrated by much lower vacancy formation energies by Ca-doping, compared with the undoped cases (Table 1), the excellent dopability of Ca in Na_3PS_4 indicates that the site occupancy of Na (the occupancy for Na1 site) could approach more readily to 0.5 where $n_c(1-n_c)$ becomes maximum, compared with the undoped Na_3PS_4 . In this context, the parabolic curve of the conductivity as a function of the amount of Ca-doping (x) in $\text{Na}_{3-2x}\text{Ca}_x\text{PS}_4$ in Figure 3e could be associated with the function of site occupancy $n_c(1-n_c)$. The similar behavior is also found in the classical example of $\text{Li}_{4-3x}\text{Al}_x\text{SiO}_4$ ($0 \leq x \leq 0.5$).⁴² Whereas the end members of solid-solution, Li_4SiO_4 and $\text{Li}_{2.5}\text{Al}_{0.5}\text{SiO}_4$ are almost insulating, the conductivity for the intermediate composition ($x = 0.25$) exhibits an optimal conductivity of $\sim 10^{-5} \text{ S cm}^{-1}$ at 100 °C.

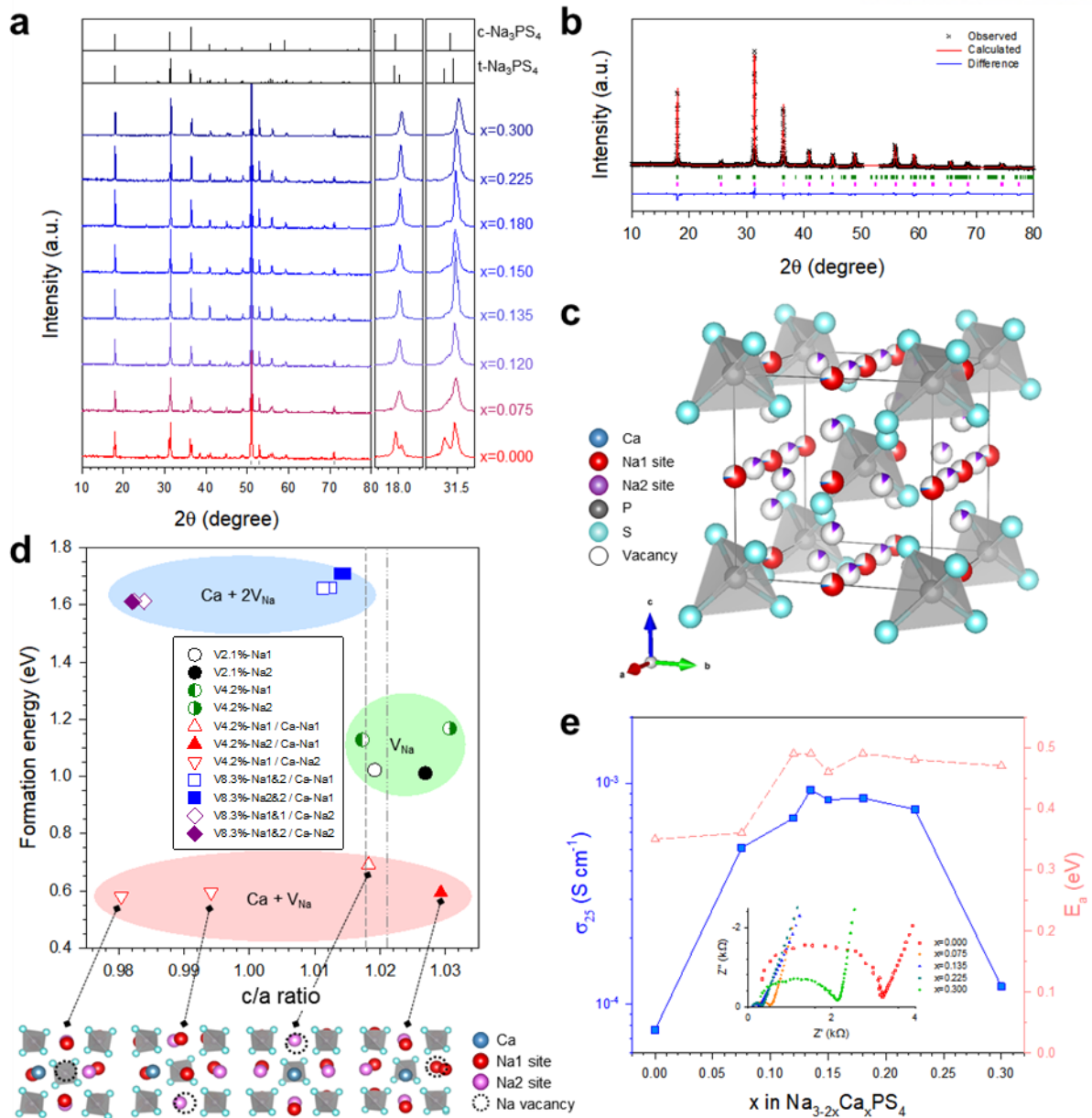


Figure 3. Characterization of Ca-doped Na₃PS₄ (Na_{3-2x}Ca_xPS₄ (0 ≤ x ≤ 0.300)) prepared at 700 °C. a) Powder XRD patterns for Na_{3-2x}Ca_xPS₄. b) X-ray Rietveld refinement profile for Na_{2.730}Ca_{0.135}PS₄. c) Crystal structure of Na_{2.730}Ca_{0.135}PS₄ with the unit cell outlined. d) Calculated formation energy as a function of c/a ratio, varied by Ca doping and V_{Na} concentration. The filled, empty, and half-filled symbols are denoted to represent vacancy positions and concentrations in Na1 or Na2 site of t-Na₃PS₄. The circles denote Na_{2.9375}PS₄ (empty or filled in black) and Na_{2.8750}PS₄ (half-filled in green). The other symbols represent concentrations of vacancy, and positions of Ca and V_{Na} for Ca-doped Na₃PS₄; Na_{2.750}Ca_{0.125}PS₄ (up and down triangle in red), Na_{2.625}Ca_{0.125}PS₄ (square in blue and diamond in violet, empty or filled). The short dashed line (---) and the dash dot line (-.-.-) indicate the c/a ratios for t-Na₃PS₄ by the experiment¹⁶ and calculation, respectively. e) Na-ion conductivities at 25 °C and activation energies for Na_{3-2x}Ca_xPS₄. Nyquist plots are shown in the inset in (e).

Table 1. Calculated vacancy formation energy for Na₃PS₄ without and with Ca-doping.

Doping	Concentration of Ca	Concentration of vacancy	Composition	Formation energy [eV]
Without Ca-doping	-	1.67%	Na _{2.9500} PS ₄	1.00
	-	2.08%	Na _{2.9375} PS ₄ ^{a)}	1.01
	-	4.17%	Na _{2.8750} PS ₄ ^{b)}	1.13
With Ca-doping	3.13%	1.67%	Na _{2.900} Ca _{0.0500} PS ₄	0.59
	6.25%	2.08%	Na _{2.875} Ca _{0.0625} PS ₄	0.58
	12.50%	4.17%	Na _{2.750} Ca _{0.1250} PS ₄ ^{c)}	0.58
	12.50%	8.33%	Na _{2.625} Ca _{0.1250} PS ₄ ^{d)}	1.61

^{a)} V2.1%-Na1(2), ^{b)} V4.2%-Na1(2), ^{c)} V4.2%-Na1(2) / Ca-Na1(2), ^{d)} V8.3%-Na1(2)&1(2) / Ca-Na1(2)

In an attempt to obtain alternative information about Na-ion dynamics, ^{23}Na solid-state NMR spectra for $t\text{-Na}_3\text{PS}_4$ and $\text{Na}_{2.730}\text{Ca}_{0.135}\text{PS}_4$ were obtained. Figure 4a displays ^{23}Na static NMR spectra recorded at various temperatures. At low temperature of 165 K, the both spectra show broad complex asymmetric signals, which are attributed to second-order quadrupolar and dipolar interactions.²⁵ As the temperature increases, the broad spectra become narrower, which is referred to motional narrowing.^{25, 43} For Ca-doped Na_3PS_4 , at 345 K the spectra shows a symmetric peak, which could be interpreted that Na-ion mobility is high enough to average out the quadrupolar and dipolar interactions. In stark contrast, $t\text{-Na}_3\text{PS}_4$ shows the asymmetric resonance signal even at high temperature of 435 K. Figure 4b shows ^{23}Na NMR spin-lattice relaxation rates ($1/T_1$) as a function of temperature. For Ca-doped Na_3PS_4 , $1/T_1$ exhibits a maximum at 360 K where the hopping frequency of Na ions is regarded to be equivalent to the Larmor frequency ω_0 .²⁵ In contrast, $1/T_1$ for $t\text{-Na}_3\text{PS}_4$ does not reach maximum at high temperature of 435 K, implying that Na-ion mobility in $t\text{-Na}_3\text{PS}_4$ at 435 K is still lower than the order of Larmor frequency.²⁵ In short, both the motional narrowing (Figure 4a) and spin-lattice relaxation rate results (Figure 4b) confirm much faster diffusion of Na ions in Ca-doped $c\text{-Na}_3\text{PS}_4$ than in $t\text{-Na}_3\text{PS}_4$, which agrees perfectly with the conductivity results (Figure 3e).

Furthermore, the activation energy for Na-ion diffusion in $t\text{-Na}_3\text{PS}_4$ and Ca-doped Na_3PS_4 , obtained from the slope of $\log[1/T_1]$ as a function of $1000/T$ (Figure 4b), appears to be 0.226 and 0.346 eV, respectively.²⁵ These values are lower than those obtained by the AC method (0.35 and 0.49 eV, respectively, Figure 3e), which is reasonable considering additional contributions such as electrode-electrolyte interfacial and grain boundary resistances for the AC method.¹⁹ Importantly, in line with the AC impedance results (Figure 3e), the abnormal behavior of higher activation energies of Na-ion diffusion for Ca-doped Na_3PS_4 than that for $t\text{-Na}_3\text{PS}_4$ is confirmed by the ^{23}Na NMR results (Figure 4b). Lastly, using the Einstein–Smoluchowski equation, a self-diffusion coefficient for Ca-doped Na_3PS_4 at 360 K, where $1/T_1$ reaches maximum, is calculated to be $1.4 \times 10^{-7} \text{ cm}^2 \text{ s}^{-1}$.²⁵ The Nernst-Einstein relation then gives the corresponding ionic conductivity of 11 mS cm^{-1} . Using the Arrhenius equation with the activation energy of 0.346 eV, a conductivity of 1.4 mS cm^{-1} at $25 \text{ }^\circ\text{C}$ was obtained (see Supporting Information for details). Despite the rough estimation, interestingly, this value is comparable to that measured by the AC method (0.94 mS cm^{-1} , Figure 3e).

In most cases for superionic conductors, enhanced ionic conductivities have been observed according to the decreased energy barriers.^{6, 44} It is general explanation that highly polarizable elements, such as S and I, as a framework constituent are advantageous for fast ionic conduction because the energy barrier could be lowered.⁴² Ceder and coworkers provided an insight that body centered cubic (bcc) anion frameworks allow direct hopping of Li ions between adjacent tetrahedral site with low energy barriers, enabling high ionic conductivities.⁶ In a recent report by Mo and coworkers, significantly lowered energy barriers by concerted migrations of multiple ions are revealed, which rationalized the

high ionic conductivities for non-bcc structured superionic conductors.⁴⁴ All the above-mentioned instances placed a strong emphasis on correlation between high conductivity and low energy barrier. In this regard, the result for Ca-doped Na_3PS_4 , namely the enhanced conductivities with the increased energy barriers, is not common.

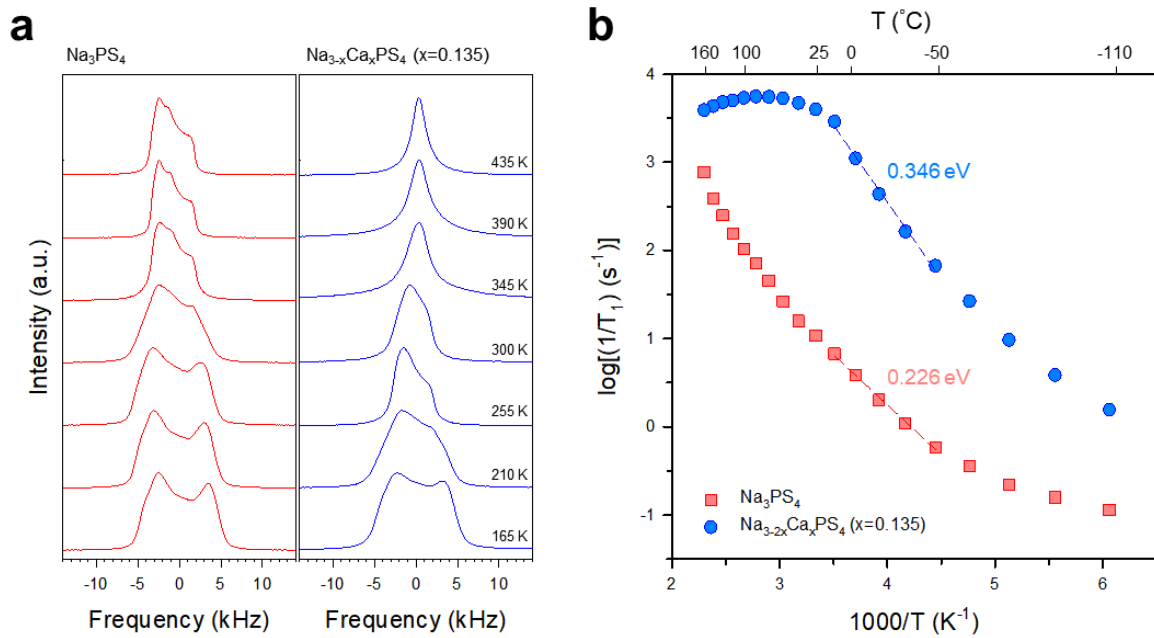


Figure 4. Results of ^{23}Na static NMR for t- Na_3PS_4 and Ca-doped cubic Na_3PS_4 ($\text{Na}_{2.730}\text{Ca}_{0.135}\text{PS}_4$). a) ^{23}Na NMR spectra and b) ^{23}Na NMR spin-lattice relaxation rate $1/T_1$ at different temperatures. Activation energies are shown in (b).

As an effort to understand this abnormal behavior of Ca-doped Na_3PS_4 , the following theoretical methods were carried out; i) the nudged elastic band (NEB) method to examine the effect of Ca^{2+} on mobility of Na^+ which is locally distributed around Ca^{2+} , ii) ab-initio molecular dynamic (MD) to analyze the averaged macroscopic effect of Ca^{2+} on the Na^+ mobility in the entire systems.

As shown in Figure 5, the Na^+ migration barriers in the out-of-plane and in-plane directions for undoped Na_3PS_4 ($\text{Na}_{2.875}\text{PS}_4$) are quite low; ~ 0.08 eV. In sharp contrast, the Na migration barriers near Ca^{2+} in the out-of-plane and in-plane directions for Ca-doped case ($\text{Na}_{2.750}\text{Ca}_{0.125}\text{PS}_4$) appears to be 2-3 times higher; 0.26 eV and 0.14 eV, respectively. Ca^{2+} has a higher positive charge than Na^+ , pushing away nearby Na^+ ions due to strong Coulomb repulsion. Thus, V_{Na} is easily formed near Ca^{2+} , and easily trapped, resulting in high migration barrier. The detailed information on the energy barriers for the other paths is summarized in Figure S6 and Table 2.

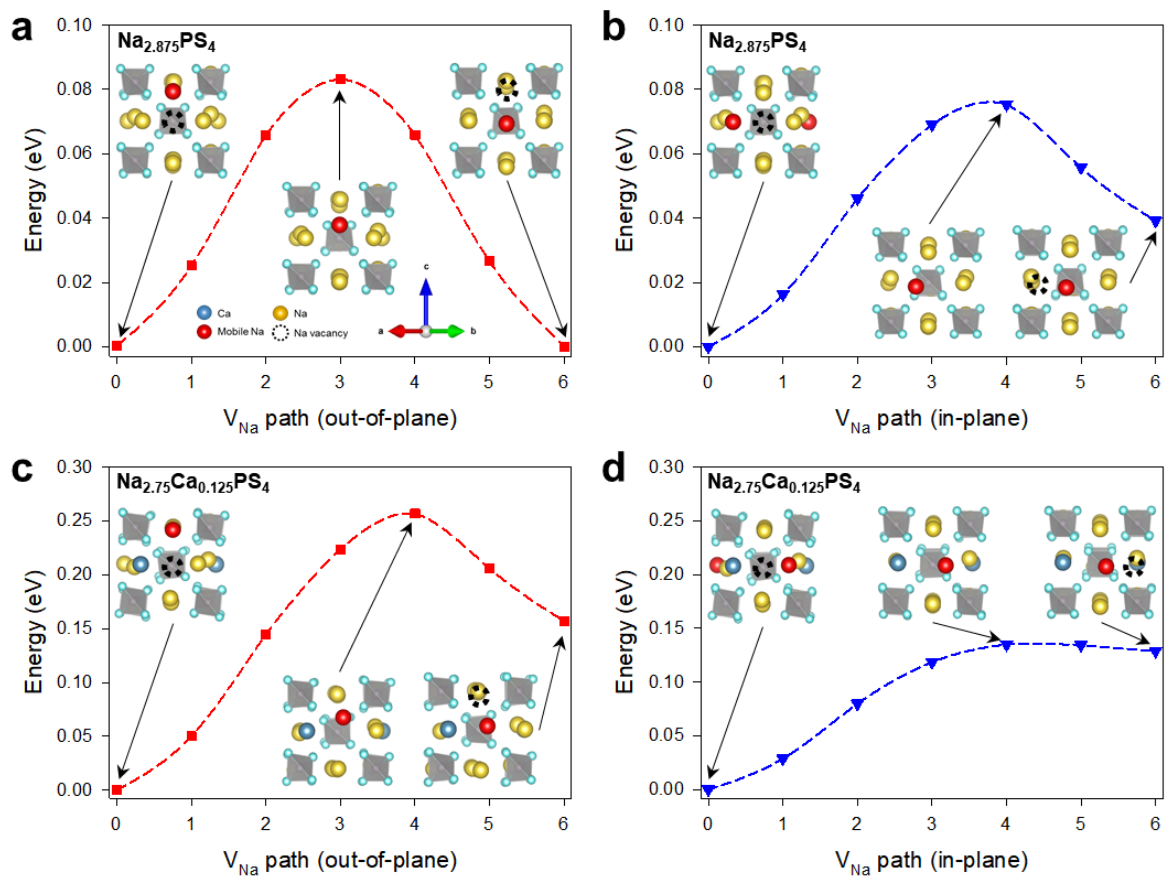


Figure 5. Calculated migration barriers for Na vacancy (V_{Na}) in the undoped and Ca-doped Na_3PS_4 . The insets show the initial, transition, and final states. a) Out-of-plane and b) in-plane migration barriers for $\text{Na}_{2.875}\text{PS}_4$. c) Out-of-plane and d) in-plane migration barriers for $\text{Na}_{2.75}\text{Ca}_{0.125}\text{PS}_4$.

Table 2. Calculated Na vacancy (V_{Na}) energy barriers for Na_3PS_4 without and with Ca-doping.

Defect type	Composition	Energy barrier [eV]
Na vacancy (in plane)	$\text{Na}_{23}\text{P}_8\text{S}_{32}$ ^{a)}	0.0753
Na vacancy (out of plane)	$(\text{Na}_{2.875}\text{PS}_4)$	0.0831
Na vacancy + Na substitution with Ca^{2+} at Na1 site (in plane)	$\text{Na}_{22}\text{Ca}_1\text{P}_8\text{S}_{32}$ ^{a)}	0.223
Na vacancy + Na substitution with Ca^{2+} at Na2 site (in plane)	$(\text{Na}_{2.750}\text{Ca}_{0.125}\text{PS}_4)$	0.135
Na vacancy + Na substitution with Ca^{2+} at Na2 site (out of plane)		0.257

^{a)} 4.17% of V_{Na} concentration

Figure 6 shows the mean square distance (MSD) of total Na at 1100 and 700 K, which are relatively high and low temperatures, respectively. As shown in Figure 6a, at 1100 K, the MSD for Ca-doped Na_3PS_4 ($\text{Na}_{2.750}\text{Ca}_{0.125}\text{PS}_4$, red) is much higher than that for pristine t- Na_3PS_4 having no V_{Na} (blue). This result confirms that the large number of V_{Na} created by Ca-doping generates Na^+ ion pathways and facilitates the Na^+ migration. This is also in line with the suggestion in previous report that the conductivity for Na_3PS_4 is governed by the vacancy rather than structure.^{14, 21, 24-25} However, when t- Na_3PS_4 has the same V_{Na} concentration without Ca doping ($\text{Na}_{2.875}\text{PS}_4$), the MSD (black) is relatively higher than that of the Ca-doped counterpart. This could be rationalized by the higher energy barrier to Na^+ migration induced by Ca^{2+} . Similar tendency is found for the Na^+ migration at 700 K. As shown in Figure 6b, the MSD for both undoped t- Na_3PS_4 ($\text{Na}_{2.875}\text{PS}_4$) and Ca-doped Na_3PS_4 ($\text{Na}_{2.750}\text{Ca}_{0.125}\text{PS}_4$) exhibits linearly increasing behaviors up to 30 ps. After 30 ps, however, the slope of Ca-doped Na_3PS_4 becomes zero, while the slope of undoped Na_3PS_4 keeps linearly increasing. This is because the thermal energy is not sufficient for Na^+ ions to migrate beyond the energy barrier created by Ca^{2+} . These MD calculations match with the trapping effect shown in the NEB results (Figures 5, S6). Detailed MSD data for other temperatures are shown in Figure S7.

In short, by the complementary analysis so far, it could be rationalized that the overall conductivity would be determined by interplay between the enhancement by the V_{Na} generated by Ca-doping and the depression by the increased energy barriers nearby the Na sites in which Ca^{2+} is occupied. It is believed that the Ca-doped Na_3PS_4 , showing the high conductivities and the high activation energies, is an exceptional case that the former prevails the latter.

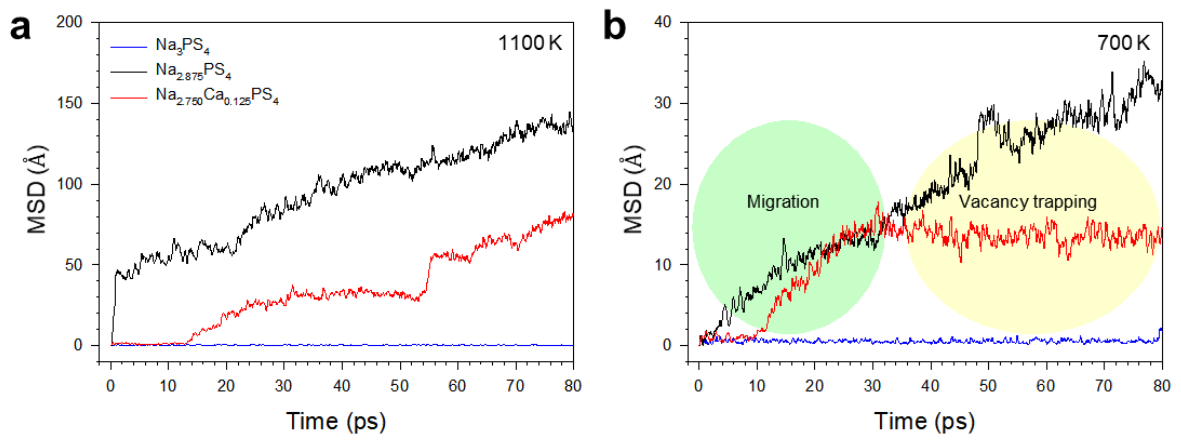


Figure 6. MSD depending on the time step for a) 1100 K and b) 700 K.

Finally, $\text{TiS}_2/\text{Na-Sn}$ ASNBs were fabricated using $\text{c-Na}_3\text{PS}_4$ (0.1 mS cm^{-1}) and Ca-doped Na_3PS_4 ($\text{Na}_{2.730}\text{Ca}_{0.135}\text{PS}_4$, 0.94 mS cm^{-1}) and cycled between 1.0-2.5 V at 30°C . Figure 7a shows the first two-cycle discharge-charge voltage profiles at $50 \mu\text{A cm}^{-2}$. The charge capacities at second cycle for the cells using $\text{c-Na}_3\text{PS}_4$ and $\text{Na}_{2.730}\text{Ca}_{0.135}\text{PS}_4$ are 191 and 205 mA h g^{-1} , respectively. These values, corresponding with extraction of 0.8 mole of Li, are not only much higher than those for the TiS_2 -based ASNBs in previous reports¹⁴⁻¹⁵ but also comparable to those for the TiS_2/Li cells using liquid electrolytes.⁸ The charge capacities for $\text{TiS}_2/\text{Na-Sn}$ cells employing $\text{c-Na}_3\text{PS}_4$ and $\text{Na}_{2.730}\text{Ca}_{0.135}\text{PS}_4$, as a function of cycle number, varied by different current densities, are also displayed in Figure 7b (voltage profiles at different current densities and different cycle numbers are shown in Figure S8). At high current densities, capacity gap varied by the solid electrolytes becomes distinct. At 0.50 mA cm^{-2} , while the $\text{TiS}_2/\text{Na-Sn}$ ASNB using $\text{c-Na}_3\text{PS}_4$ shows negligible capacities of 11 mA h g^{-1} , the one using $\text{Na}_{2.730}\text{Ca}_{0.135}\text{PS}_4$ retains 20% capacity at $50 \mu\text{A cm}^{-2}$ (40 mA h g^{-1}). Moreover, capacity retention for $\text{TiS}_2/\text{Na-Sn}$ ASNBs employing $\text{Na}_{2.730}\text{Ca}_{0.135}\text{PS}_4$ after 25 cycles is 91.9% which is contrasted by 91.0% for the case using $\text{c-Na}_3\text{PS}_4$. Overall, the decent electrochemical performances for $\text{TiS}_2/\text{Na-Sn}$ ASNBs using $\text{Na}_{2.730}\text{Ca}_{0.135}\text{PS}_4$ highlights the high conductivity of Ca-doped Na_3PS_4 and the good compatibility between TiS_2 and Ca-doped Na_3PS_4 .

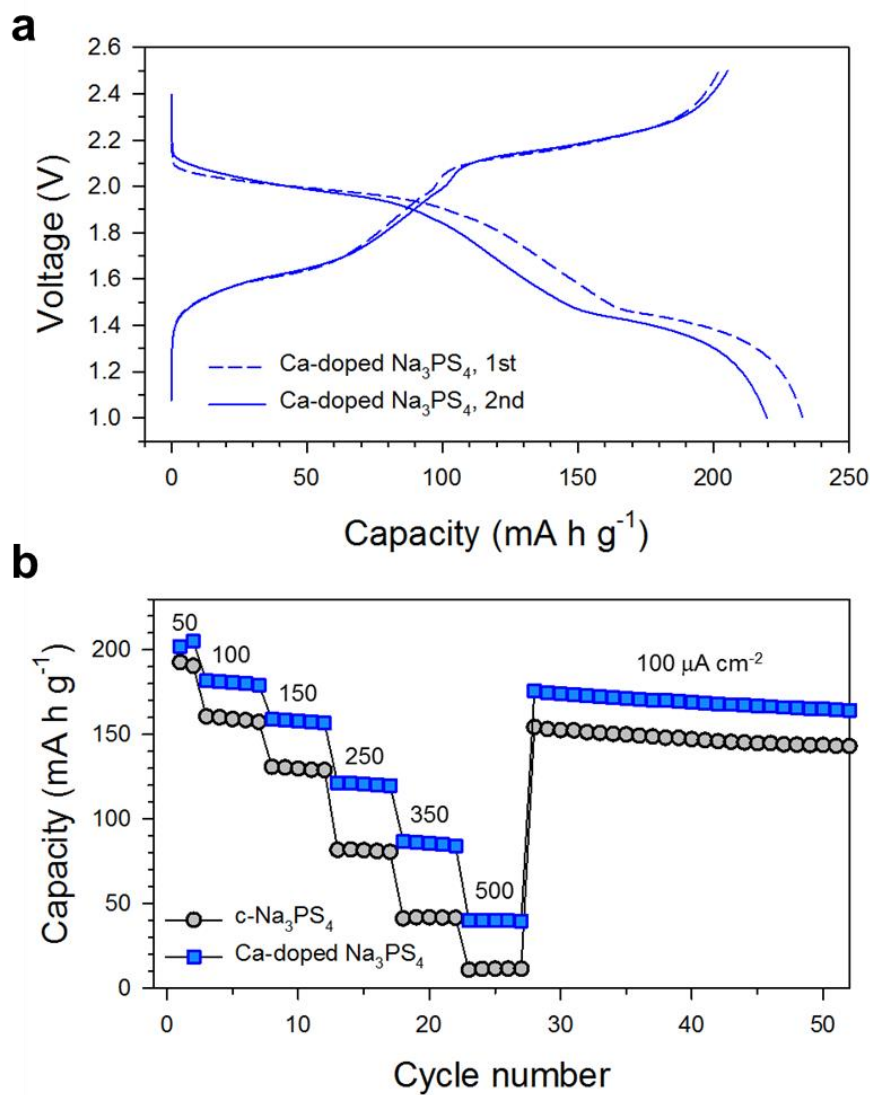


Figure 7. Electrochemical performance of TiS₂/Na-Sn ASNBs using c-Na₃PS₄ and Ca-doped Na₃PS₄ (Na_{2.730}Ca_{0.135}PS₄) at 30 °C. a) First two-cycle discharge-charge voltage profiles at 50 μA cm⁻² (0.06C). b) Charge capacity as a function of cycle number, varied by different current densities. The numbers are the current densities in μA cm⁻².

V. Conclusion

In summary, the highly conductive $\text{Na}_{3-2x}\text{Ca}_x\text{PS}_4$ solid electrolytes were synthesized ($x = 0.135$, $\sim 1 \text{ mS cm}^{-1}$ at room temperature) with a range of nominal compositions of $0.000 \leq x \leq 0.450$. From the structural analysis using XRD, Rietveld refinement and DFT, the tetragonal-to-cubic phase transition with Ca doping was identified ($\overline{P4}2_1c \rightarrow \overline{I}43m$). Furthermore, the abnormal behavior that the activation energy is increased with high ionic conductivity was studied by DFT, NEB, MD calculations and NMR analysis. Finally, the high capacity and stable cycling performance of $\text{TiS}_2/\text{Na-Sn}$ ASNBs using $\text{Na}_{3-2x}\text{Ca}_x\text{PS}_4$ were demonstrated.

VI. Supporting information

6.1 Conductivity from ^{23}Na NMR results

At which the spin-lattice relaxation rate ($1/T_1$) is maximum (at 360 K), jump frequency for Na ions ($1/\tau$) is regarded to be equivalent to the Lamor frequency ω_0 (Equation S1).

$$1/\tau = \omega_0 \quad (\text{S1})$$

$$\omega_0 = \gamma B_0 \quad (\text{S2})$$

where γ is the magnetogyric ratio (for ^{23}Na , $70.761 \times 10^6 \text{ rad s}^{-1} \text{ T}^{-1}$), B_0 is 9.4 T.

Thus, τ is calculated to be $1.50 \times 10^{-9} \text{ s}$ at 360 K (or $1/\tau$ is calculated to be $6.65 \times 10^8 \text{ s}^{-1}$).

Using the Einstein-Smoluchowski equation (Equation S3), the self-diffusion coefficient (D_{sf}) is obtained to be $1.4 \times 10^{-7} \text{ cm}^2 \text{ s}^{-1}$ at 360 K.

$$D_{sf} = a^2/(6\tau) \quad (\text{S3})$$

where a is a jump distance, assuming 3.5 \AA based on the distance between the Na1 sites.

The Nernst-Einstein relation is given in Equation S4.

$$\sigma = Nq^2D_c/(k_B T) \quad (\text{S4})$$

where N is the charge carrier density, for $\text{Na}_{2.730}\text{Ca}_{0.135}\text{PS}_4$, $5.46/(6.975 \times 10^{-8} \text{ cm})^3 = 1.61 \times 10^{22} \text{ cm}^{-3}$, q is the elementary charge (For Na^+ , $1.602 \times 10^{-19} \text{ C}$), k_B : the Boltzmann constant, $1.380 \times 10^{-23} \text{ J K}^{-1}$, T is 360 K, D_c is the conductivity diffusion coefficient.

Assuming f/H_R is 1 in Equation S5, Equation S4 relates the conductivity (σ) with the self-diffusion coefficient (D_{sf}) (Equation S6). Then, the conductivity (σ) is obtained to be $1.1 \times 10^{-2} \text{ S cm}^{-1}$ at 360 K.

$$D_c = (f/H_R)D_{sf} \quad (\text{S5})$$

where f is the correlation factor, H_R is the Haven ratio.

$$\sigma = Nq^2D_{sf}/(k_B T) \quad (\text{S6})$$

By the Arrhenius equation (Equation 1), the conductivity at $25 \text{ }^\circ\text{C}$ is obtained to be $1.4 \times 10^{-3} \text{ S cm}^{-1}$ by applying the E_a value of 0.346 eV .

6.2 Formation energy from DFT

The vacancy formation energy for t-Na₃PS₄ depending on Ca²⁺ ion and vacancy concentrations are listed in the Table 1. The calculations for all the possible configurations were performed. Among them, the most stable structures were selected to calculate their formation energies in Table 1.

The vacancy formation energies were calculated using the formular presented by Wei et al.⁴⁵

$$E_f[A] = E_{\text{tot}}[A] - E_{\text{tot}}[\text{bulk}] - \sum_i n_i \mu_i \quad (\text{S7})$$

where $E_{\text{tot}}[A]$ is the calculated total energy of the system with the vacancy and Ca ion. And $E_{\text{tot}}[\text{bulk}]$ is the calculated total energy of the system without the vacancy and Ca ion respectively. μ_i indicates the atomic chemical potential of species i that varies based on different experimental environment (Table S19). n_i is the number of atoms of species i , added ($n_i > 0$) or removed ($n_i < 0$) from the pristine structure with no defect.

6.3 Supporting figures

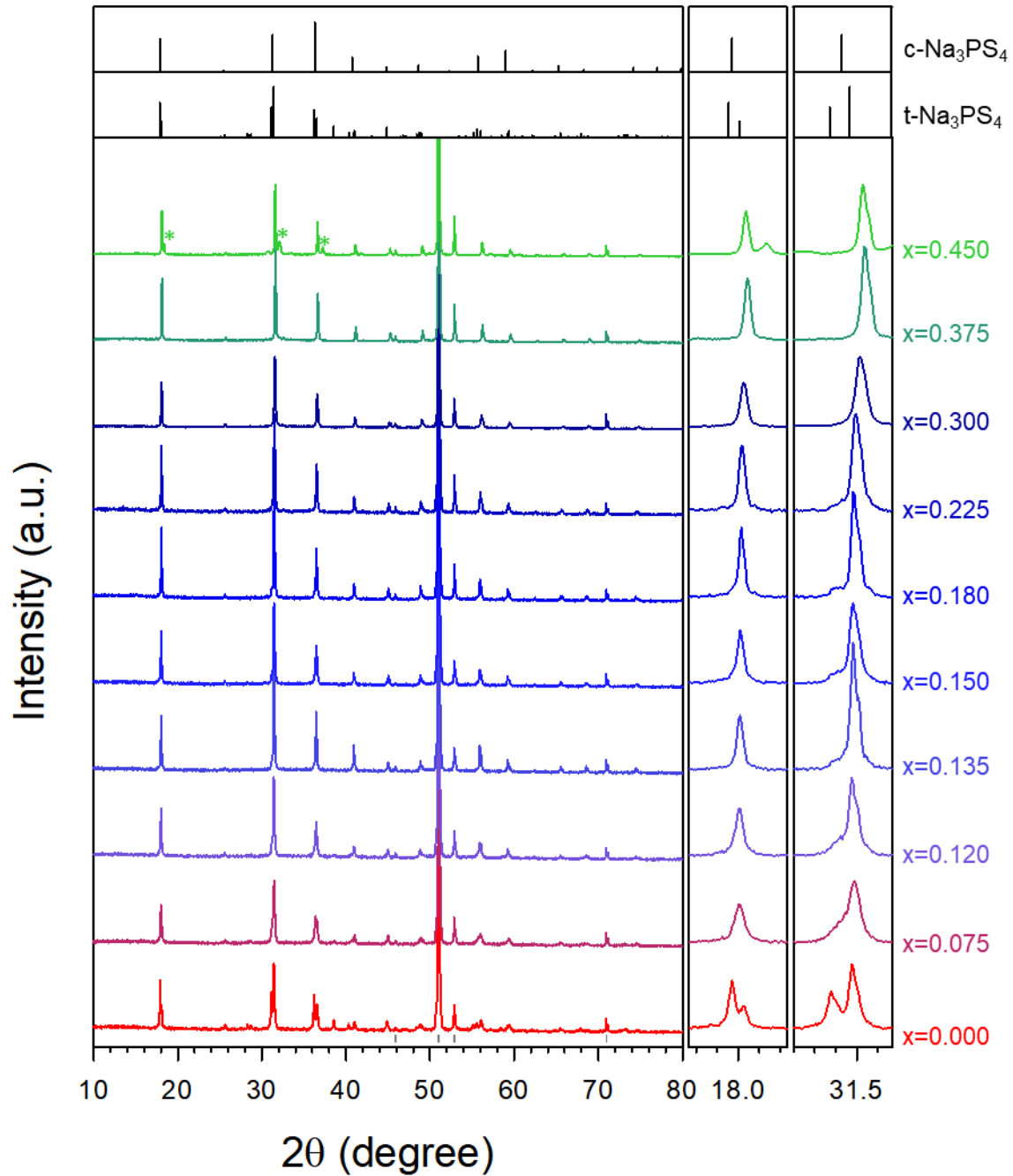


Figure S1. Powder XRD patterns for $\text{Na}_{3-2x}\text{Ca}_x\text{PS}_4$ prepared at $700\text{ }^\circ\text{C}$. Unknown peaks are denoted ‘*’.

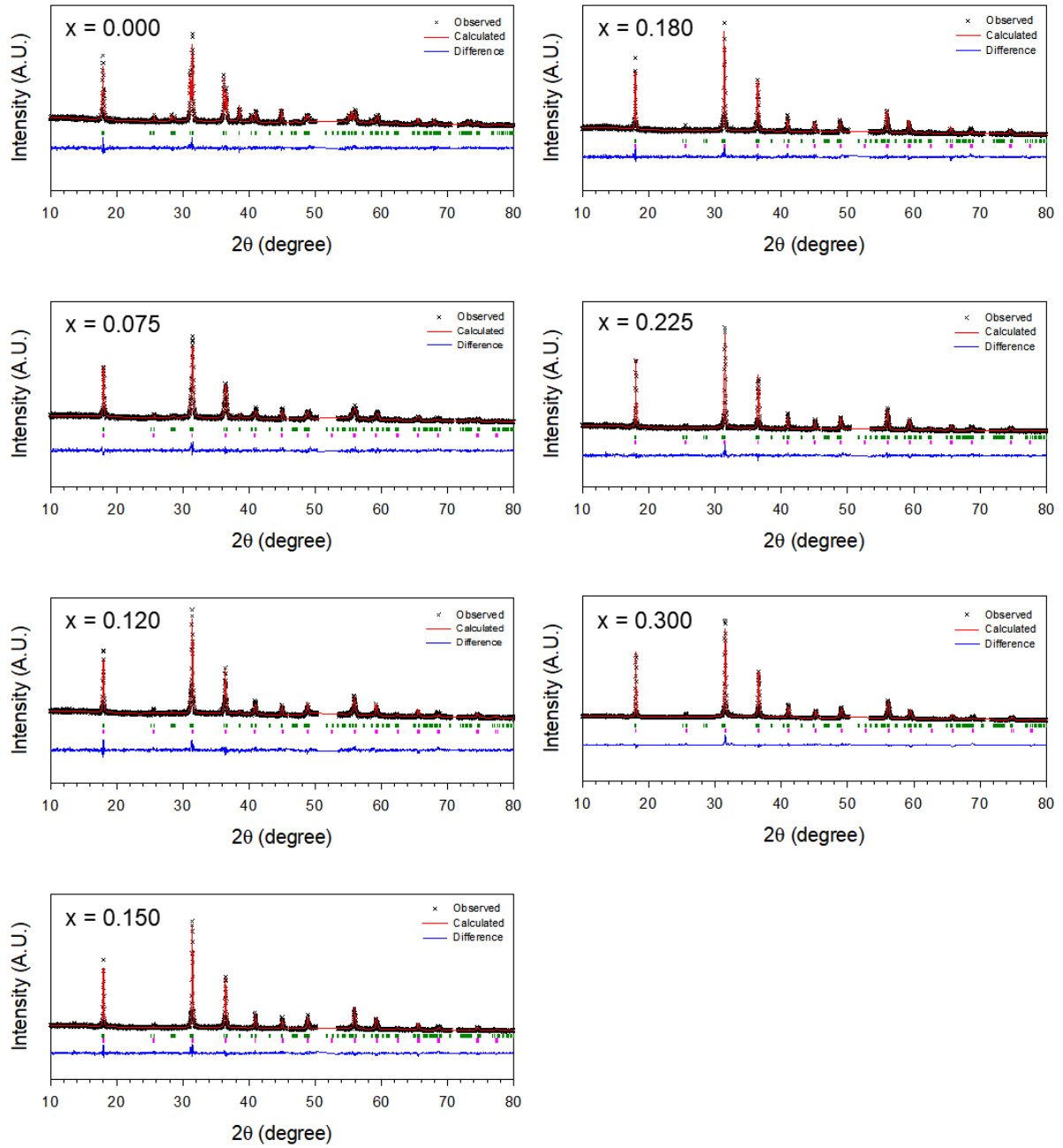


Figure S2. X-ray Rietveld refinement profiles for $\text{Na}_{3-2x}\text{Ca}_x\text{PS}_4$ prepared at $700\text{ }^\circ\text{C}$.

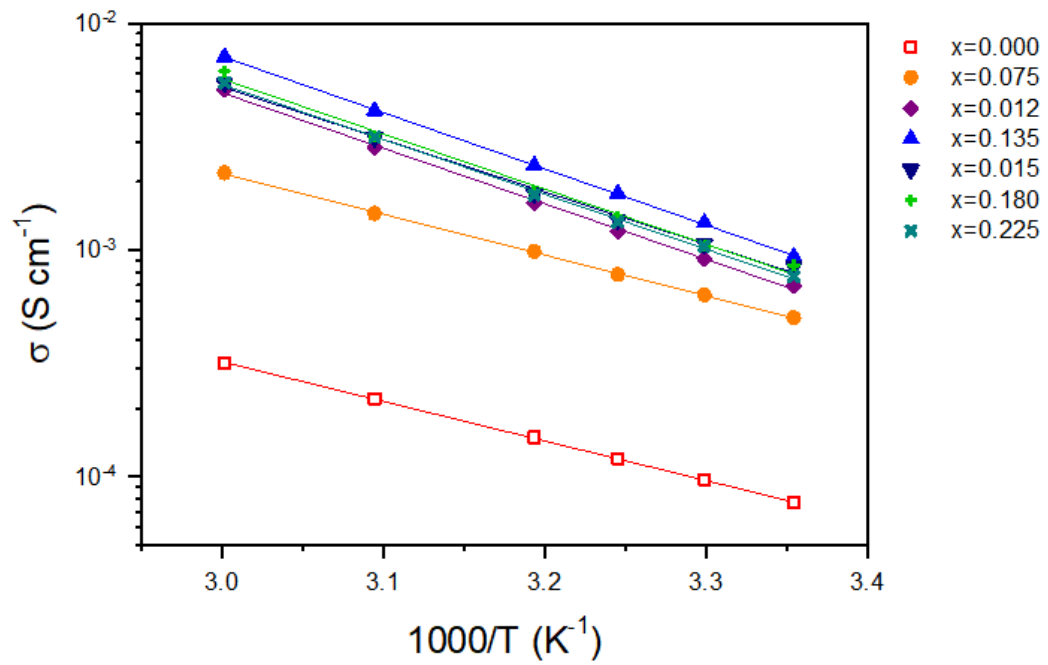


Figure S3. Arrhenius plots of Na-ion conductivities for $\text{Na}_{3-2x}\text{Ca}_x\text{PS}_4$ prepared at 700°C .

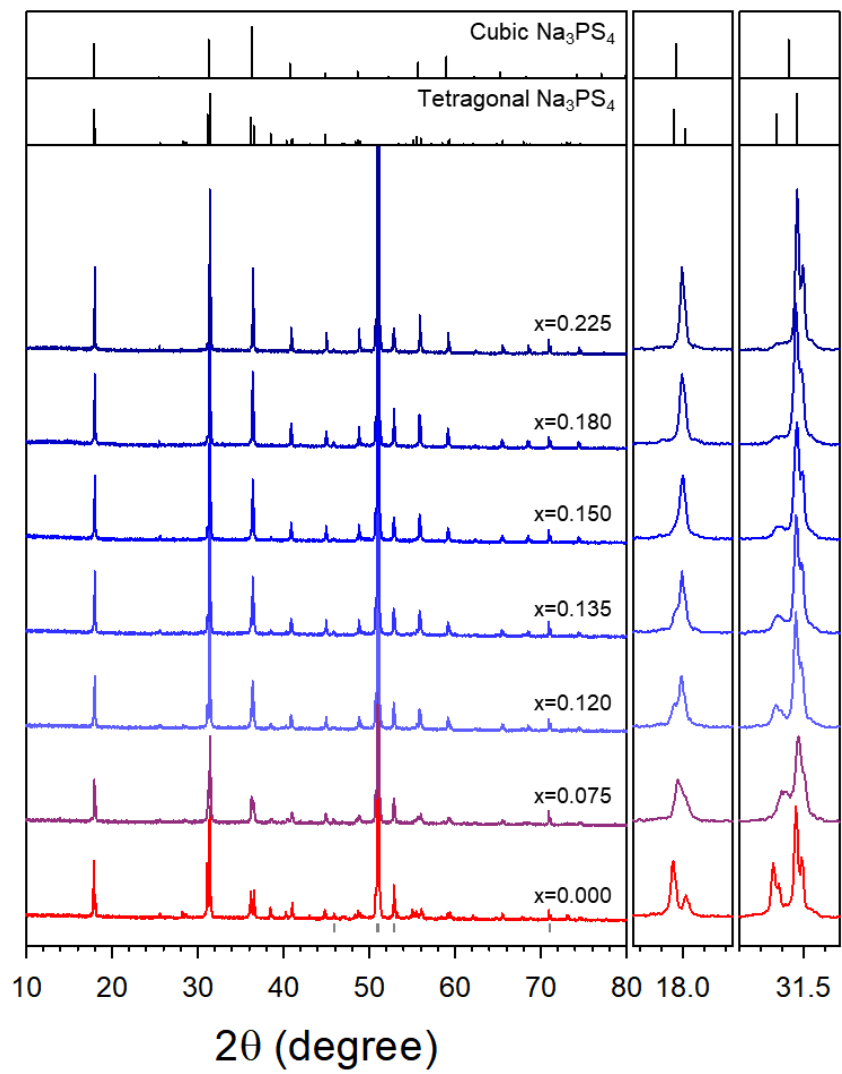


Figure S4. XRD patterns for $\text{Na}_{3-2x}\text{Ca}_x\text{PS}_4$ prepared at $550\text{ }^\circ\text{C}$.

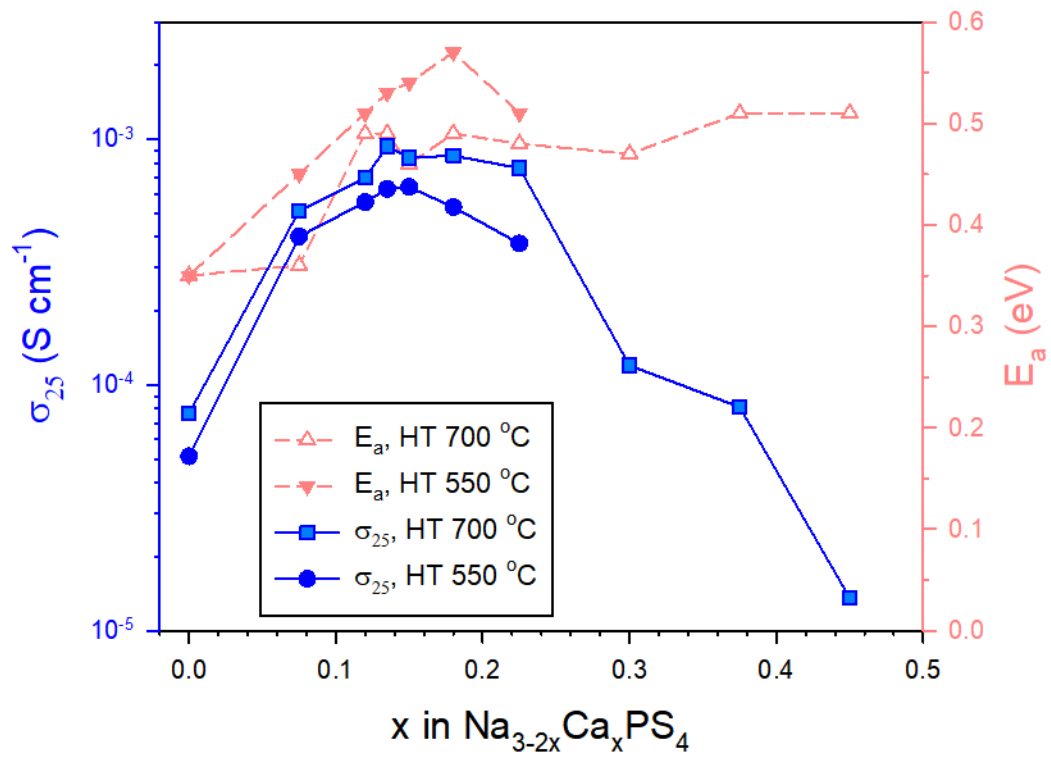


Figure S5. Conductivities and activation energies at 25 °C for Na_{3-2x}Ca_xPS₄ prepared at 700 °C and 550 °C.

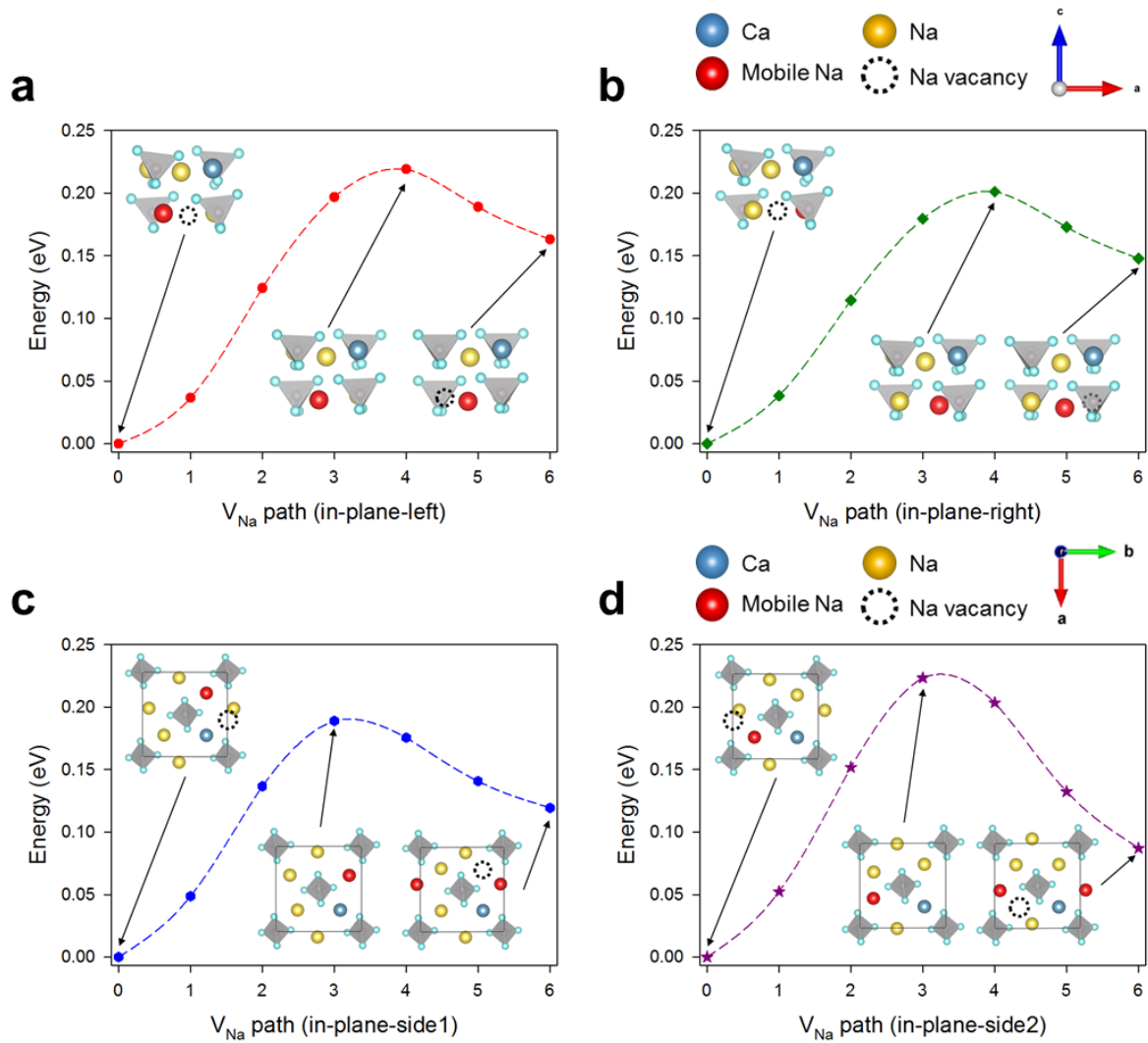


Figure S6. Calculated migration barriers for Na vacancy (V_{Na}) in the Na_3PS_4 ($Na_{2.750}Ca_{0.125}PS_4$). The inset shows the initial, transition, and final states. Migration barriers on the plane under the Ca^{2+} ion (a, b) and on the plane containing Ca^{2+} ion (c, d).

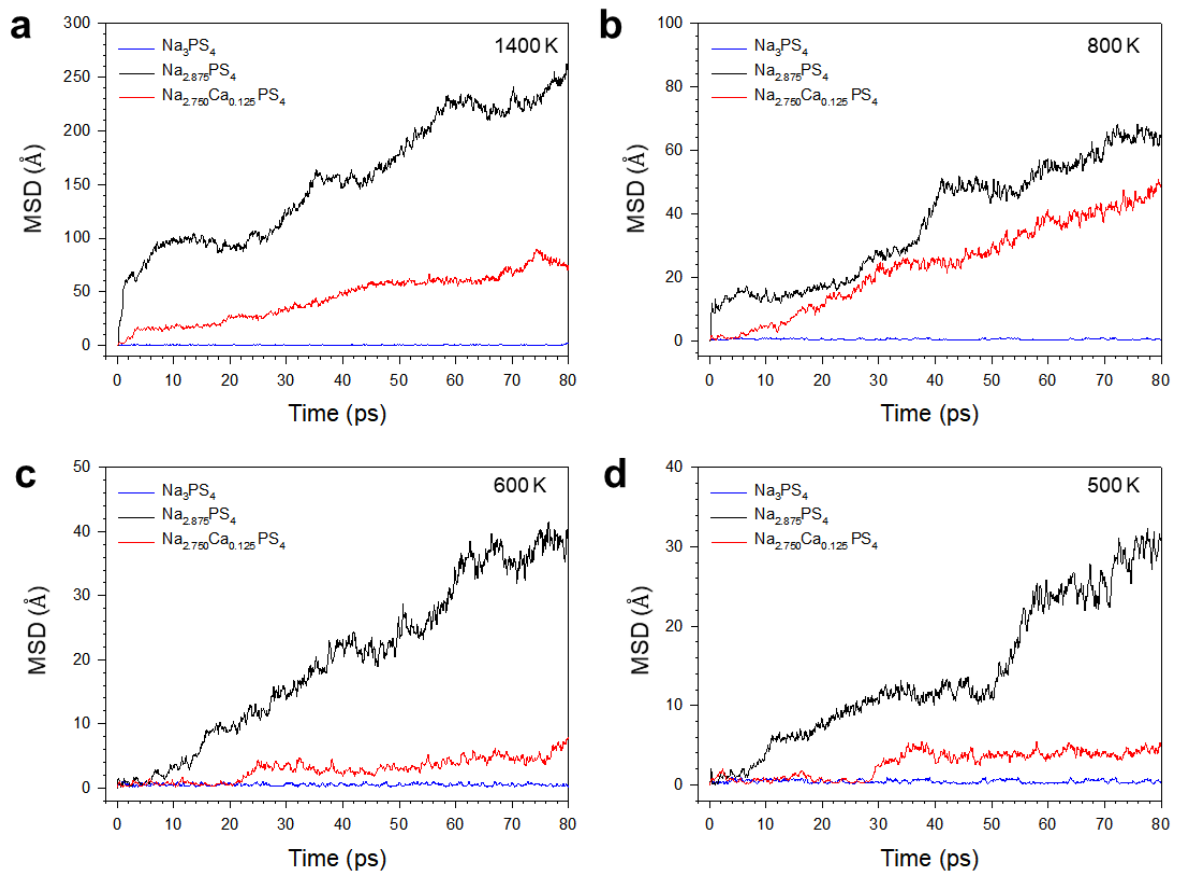


Figure S7. MSD depending on the time step for a) 1400 K, b) 800 K, c) 600 K, and d) 500 K.

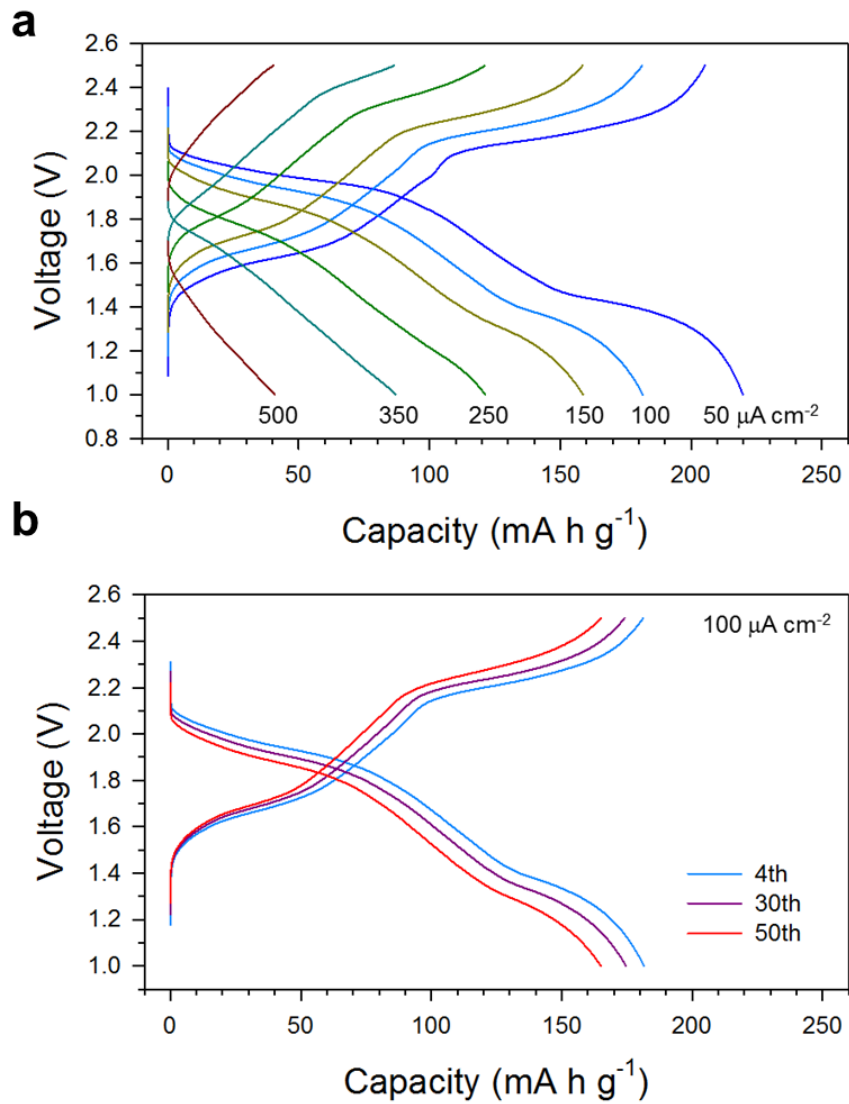


Figure S8. Discharge-charge voltage profiles for $\text{TiS}_2/\text{Na-Sn}$ ASNBs employing $\text{Na}_{2.730}\text{Ca}_{0.135}\text{PS}_4$.

6.4 Supporting tables

Table S1. Crystallographic information for $\text{Na}_{3-2x}\text{Ca}_x\text{PS}_4$ prepared at 700 °C, obtained by the Rietveld analysis.

x		a (Å)	c (Å)	R_{wp}	V (Å ³)	Phase fraction of c- Na_3PS_4 [wt%]
For nominal composition	For Ca-doped c- Na_3PS_4 phase					
0.000	-	6.9555	7.0887	0.0984	342.95	-
0.075	0.112	6.9803	6.9803	0.1008	340.11	67.7(5)
0.120	0.171	6.9773	6.9773	0.1065	339.67	70.6(4)
0.135	0.148	6.9768	6.9768	0.0637	339.61	91.7(1)
0.150	0.166	6.9750	6.9750	0.1085	339.34	90.5(1)
0.180	0.212	6.9723	6.9723	0.1024	338.94	85.8(3)
0.225	0.245	6.9695	6.9695	0.1096	338.54	92.2(1)
0.300	0.300	6.9516	6.9516	0.0651	335.93	100

Table S2. Crystallographic data and Rietveld refinement results for the sample with $x = 0.000$ for $\text{Na}_{3-2x}\text{Ca}_x\text{PS}_4$ prepared at $700\text{ }^\circ\text{C}$.

Crystal System	Tetragonal					
Space Group	P-4 ₂ c (No. 114)					
Lattice Parameter, Volume, Z	a = 6.9555(3) Å, c = 7.0887(4) Å V = 342.95(4) Å ³ , Z = 2					
Atoms	x	y	z	Wyckoff	Occupancy	U _{iso}
Na1	0	0.5	0.4234(10)	4d	1	0.034(3)
Na2	0	0	0	2a	1	0.036(5)
P	0	0	0.5	2b	1	0.025(3)
S	0.3129(5)	0.3460(5)	0.1656(5)	8e	1	0.024(1)

*R_p : 0.0757, R_{wp} : 0.0984, R_{exp} : 0.0856, R(F²) : 0.1951, $\chi^2 = 1.327$

Table S3. Selected interatomic distances and angles for the sample with $x = 0.000$ for $\text{Na}_{3-2x}\text{Ca}_x\text{PS}_4$ prepared at $700\text{ }^\circ\text{C}$.

Selected interatomic distance (Å)			
Na1-S	3.037(5) × 2	Na2-S	3.451(4) × 4
	2.972(6) × 2		2.908(4) × 4
	2.808(4) × 2		
P-S	2.054(3) × 4		
Selected interatomic angles (°)			
S-P-S	110.3(2) × 2		
	109.1(1) × 4		

Table S4. Crystallographic data and Rietveld refinement results for the sample with $x = 0.075$ for $\text{Na}_{3-2x}\text{Ca}_x\text{PS}_4$ prepared at 700 °C.

Crystal System	Cubic					
Space Group	I -4 3 m (No. 217)					
Lattice Parameter, Volume, Z	a = 6.9803(3) Å V = 340.11(4) Å ³ , Z = 2					
Atoms	x	y	z	Wyckoff	Occupancy	U _{iso}
Na1	0.5	0.5	0	6b	0.697(4)	0.036(4)
Na2	0.75	0.5	0	12d	0.115(11)	0.036(4)
Ca	0.5	0.5	0	6b	0.0373	0.036(4)
P	0	0	0.5	2a	1	0.020(5)
S	0.1726(4)	0.1726(4)	0.1726(4)	8c	1	0.022(3)

* R_p : 0.0793, R_{wp} : 0.1008, R_{exp} : 0.0883, $R(F^2)$: 0.1991, $\chi^2 = 1.601$

Table S5. Selected interatomic distances and angles for the sample with $x = 0.075$ for $\text{Na}_{3-2x}\text{Ca}_x\text{PS}_4$ prepared at 700 °C.

Selected interatomic distance (Å)			
Na1-S	3.449(3) × 4	Ca-S	3.449(3) × 4
	2.851(1) × 4		2.851(1) × 4
Na2-S	2.640(2) × 4	P-S	2.086(5) × 4
Selected interatomic angles (°)			
S-P-S	109.471(3) × 2		
	109.471(2) × 4		

Table S6. Crystallographic data and Rietveld refinement results for the sample with $x = 0.120$ for $\text{Na}_{3-2x}\text{Ca}_x\text{PS}_4$ prepared at $700\text{ }^\circ\text{C}$.

Crystal System	Cubic					
Space Group	I -4 3 m (No. 217)					
Lattice Parameter, Volume, Z	a = 6.9773(1) Å V = 339.67(2) Å ³ , Z = 2					
Atoms	X	y	z	Wyckoff	Occupancy	U _{iso}
Na1	0.5	0.5	0	6b	0.682(3)	0.036(3)
Na2	0.75	0.5	0	12d	0.100(10)	0.036(3)
Ca	0.5	0.5	0	6b	0.0570	0.036(3)
P	0	0	0	2a	1	0.030(4)
S	0.1691(4)	0.1691(4)	0.1691(4)	8c	1	0.019(2)

* R_p : 0.0821, R_{wp} : 0.1065, R_{exp} : 0.0865, $R(F^2)$: 0.3357, $\chi^2 = 1.757$

Table S7. Selected interatomic distances and angles for the sample with $x = 0.120$ for $\text{Na}_{3-2x}\text{Ca}_x\text{PS}_4$ prepared at $700\text{ }^\circ\text{C}$.

Selected interatomic distance (Å)			
Na1-S	3.472(3) × 4	Ca-S	3.472(3) × 4
	2.849(1) × 4		2.849(1) × 4
Na2-S	2.654(2) × 4	P-S	2.043(5) × 4
Selected interatomic angles (°)			
S-P-S	109.471(1) × 6		

Table S8. Crystallographic data and Rietveld refinement results for the sample with $x = 0.135$ for $\text{Na}_{3-2x}\text{Ca}_x\text{PS}_4$ prepared at 700 °C.

Crystal System	Cubic					
Space Group	I -4 3 m (No. 217)					
Lattice Parameter, Volume, Z	a = 6.9768(1) Å V = 339.61(1) Å ³ , Z = 2					
Atoms	x	y	z	Wyckoff	Occupancy	U _{iso}
Na1	0.5	0.5	0	6b	0.693(1)	0.032(1)
Na2	0.75	0.5	0	12d	0.105(3)	0.032(1)
Ca	0.5	0.5	0	6b	0.0493	0.032(1)
P	0	0	0	2a	1	0.026(1)
S	0.1708(1)	0.1708(1)	0.1708(1)	8c	1	0.026(1)

* R_p : 0.0473, R_{wp} : 0.0637, R_{exp} : 0.0406, $R(F^2)$: 0.2423, $\chi^2 = 2.470$

Table S9. Selected interatomic distances and angles for the sample with $x = 0.135$ for $\text{Na}_{3-2x}\text{Ca}_x\text{PS}_4$ prepared at 700 °C.

Selected interatomic distance (Å)			
Na1-S	3.460(1) × 4	Ca-S	3.460(1) × 4
	2.849(1) × 4		2.849(1) × 4
Na2-S	2.646(1) × 4	P-S	2.064(2) × 4
Selected interatomic angles (°)			
S-P-S	109.471(1) × 2		
	109.471(0) × 4		

Table S10. Crystallographic data and Rietveld refinement results for the sample with $x = 0.150$ for $\text{Na}_{3-2x}\text{Ca}_x\text{PS}_4$ prepared at $700\text{ }^\circ\text{C}$.

Crystal System	Cubic					
Space Group	I -4 3 m (No. 217)					
Lattice Parameter, Volume, Z	a = 6.9750(1) Å V = 339.34(2) Å ³ , Z = 2					
Atoms	x	y	z	Wyckoff	Occupancy	U _{iso}
Na1	0.5	0.5	0	6b	0.682(4)	0.033(2)
Na2	0.75	0.5	0	12d	0.101(6)	0.033(2)
Ca	0.5	0.5	0	6b	0.0553	0.033(2)
P	0	0	0	2a	1	0.026(3)
S	0.1703(3)	0.1703(3)	0.1703(3)	8c	1	0.026(2)

* R_p : 0.0817, R_{wp} : 0.1085, R_{exp} : 0.0872, $R(F^2)$: 0.2405, $\chi^2 = 1.553$

Table S11. Selected interatomic distances and angles for the sample with $x = 0.150$ for $\text{Na}_{3-2x}\text{Ca}_x\text{PS}_4$ prepared at $700\text{ }^\circ\text{C}$.

Selected interatomic distance (Å)			
Na1-S	3.463(2) × 4	Ca-S	3.463(2) × 4
	2.848(1) × 4		2.848(1) × 4
Na2-S	2.648(1) × 4	P-S	2.057(3) × 4
Selected interatomic angles (°)			
S-P-S	109.471(1) × 6		

Table S12. Crystallographic data and Rietveld refinement results for the sample with $x = 0.180$ for $\text{Na}_{3-2x}\text{Ca}_x\text{PS}_4$ prepared at $700\text{ }^\circ\text{C}$.

Crystal System	Cubic					
Space Group	I -4 3 m (No. 217)					
Lattice Parameter, Volume, Z	a = 6.9723(1) Å V = 338.94(2) Å ³ , Z = 2					
Atoms	x	y	z	Wyckoff	Occupancy	U _{iso}
Na1	0.5	0.5	0	6b	0.651(3)	0.034(4)
Na2	0.75	0.5	0	12d	0.101(10)	0.034(4)
Ca	0.5	0.5	0	6b	0.0707	0.034(4)
P	0	0	0	2a	1	0.020(4)
S	0.1705(4)	0.1705(4)	0.1705(4)	8c	1	0.018(2)

* R_p : 0.0782, R_{wp} : 0.1024, R_{exp} : 0.0845, $R(F^2)$: 0.2573, $\chi^2 = 2.804$

Table S13. Selected interatomic distances and angles for the sample with $x = 0.180$ for $\text{Na}_{3-2x}\text{Ca}_x\text{PS}_4$ prepared at $700\text{ }^\circ\text{C}$.

Selected interatomic distance (Å)			
Na1-S	3.460(3) × 4	Ca-S	3.460(3) × 4
	2.847(1) × 4		2.847(1) × 4
Na2-S	2.646(2) × 4	P-S	2.059(5) × 4
Selected interatomic angles (°)			
S-P-S	109.471(2) × 2		
	109.471(1) × 4		

Table S14. Crystallographic data and Rietveld refinement results for the sample with $x = 0.225$ for $\text{Na}_{3-2x}\text{Ca}_x\text{PS}_4$ prepared at 700 °C.

Crystal System	Cubic					
Space Group	I -4 3 m (No. 217)					
Lattice Parameter, Volume, Z	a = 6.9695(1) Å V = 338.54(2) Å ³ , Z = 2					
Atoms	x	y	z	Wyckoff	Occupancy	U _{iso}
Na1	0.5	0.5	0	6b	0.628(2)	0.036(3)
Na2	0.75	0.5	0	12d	0.104(8)	0.036(3)
Ca	0.5	0.5	0	6b	0.0817	0.036(3)
P	0	0	0	2a	1	0.021(3)
S	0.1710(3)	0.1710(3)	0.1710(3)	8c	1	0.020(2)

* R_p : 0.0837, R_{wp} : 0.1096, R_{exp} : 0.0907, $R(F^2)$: 0.2736, $\chi^2 = 1.813$

Table S15. Selected interatomic distances and angles for the sample with $x = 0.225$ for $\text{Na}_{3-2x}\text{Ca}_x\text{PS}_4$ prepared at 700 °C.

Selected interatomic distance (Å)			
Na1-S	3.455(2) × 4	Ca-S	3.455(2) × 4
	2.846(1) × 4		2.846(1) × 4
Na2-S	2.642(1) × 4	P-S	2.064(4) × 4
Selected interatomic angles (°)			
S-P-S	109.471(1) × 6		

Table S16. Crystallographic data and Rietveld refinement results for the sample with $x = 0.300$ for $\text{Na}_{3-2x}\text{Ca}_x\text{PS}_4$ prepared at $700\text{ }^\circ\text{C}$.

Crystal System	Cubic					
Space Group	I -4 3 m (No. 217)					
Lattice Parameter, Volume, Z	a = 6.9516(1) Å V = 335.93(1) Å ³ , Z = 2					
Atoms	x	y	z	Wyckoff	Occupancy	U _{iso}
Na1	0.5	0.5	0	6b	0.591(1)	0.039(2)
Na2	0.75	0.5	0	12d	0.108(4)	0.039(2)
Ca	0.5	0.5	0	6b	0.100	0.039(2)
P	0	0	0	2a	1	0.025(2)
S	0.1712(2)	0.1712(2)	0.1712(2)	8c	1	0.020(1)

* R_p : 0.0496, R_{wp} : 0.0651, R_{exp} : 0.0411, $R(F^2)$: 0.2929, $\chi^2 = 2.560$

Table S17. Selected interatomic distances and angles for the sample with $x = 0.300$ for $\text{Na}_{3-2x}\text{Ca}_x\text{PS}_4$ prepared at $700\text{ }^\circ\text{C}$.

Selected interatomic distance (Å)			
Na1-S	3.445(1) × 4	Ca-S	3.445(1) × 4
	2.839(1) × 4		2.839(1) × 4
Na2-S	2.635(1) × 4	P-S	2.061(2) × 4
Selected interatomic angles (°)			
S-P-S	109.471(1) × 2		
	109.471(0) × 4		

Table S18. Characteristics for sulfide Na superionic conductors.

Composition	Structure	σ_{25} [mS cm ⁻¹]	E_a [eV]	Density [cm ³ g ⁻¹]	Notes	Ref
Na ₃ PS ₄	Tetragonal	0.001 0.077 ^{a)}	0.416 0.35 ^{a)}	2.22		<i>J. Solid-State Chem</i> 1992 ¹⁶
Na ₃ PS ₄	Cubic	0.2 or 0.46	0.197	2.21		<i>Nat. Commun.</i> 2011; <i>JPS</i> 2014 ¹⁰
94Na ₃ PS ₄ ·6Na ₄ SiS ₄	Cubic	0.74	0.238	2.21		<i>RSC Adv.</i> 2014 ¹¹
Na ₃ PSe ₄	Cubic	1.16	0.21	3.53		<i>Adv. Energy Mater.</i> 2015 ¹²
Na ₁₀ SnP ₂ S ₁₂	Tetragonal	0.356	0.356	2.77		<i>Nat. Commun.</i> 2016 ⁴⁶
Na ₃ SbS ₄	Tetragonal	1.1 ^{b)} 0.1-0.2 ^{c)}	0.20 ^{b)} 0.30-0.37 ^{c)}	2.85	Dry-air stable Solution-processable	<i>Angew. Chem. Int. Ed.</i> 2016 ¹³
Na _{2.9375} PS _{3.9375} Cl _{0.0625}	Tetragonal	1 ^{d)}	0.249	2.19		<i>Sci. Rep.</i> 2016 ¹⁴
Na ₃ P _{0.62} As _{0.38} S ₄	Tetragonal	1.46	0.256	2.34		<i>Adv. Mater.</i> 2017 ¹⁵
Na _{2.730} Ca _{0.135} PS ₄	Cubic	0.94	0.49 ^{e)} 0.346 ^{f)}	2.22		This work

^{a)} obtained in this work; ^{b)} obtained from solid-state synthesized samples; ^{c)} obtained from solution-processed samples; ^{d)} obtained using spark-plasma-sintered pellets; ^{e)} obtained by AC method; ^{f)} obtained by ²³Na NMR

Table S19. Chemical potential of Na and Ca for decomposed products.

Defect type	Element	Chemical potential	Decomposed products
Vacancy	Na	-2.866 eV	$\text{Na}_3\text{PS}_4 + \text{NaS} + \text{P}$
Interstitial	Ca	-5.814 eV	$\text{CaS} + \text{Na} + \text{Na}_2\text{S} + \text{Na}_3\text{P} + \text{Na}_3\text{P}_{11} + \text{Na}_3\text{PS}_4 + \text{NaP} + \text{P}$

References

1. Goodenough, J. B.; Kim, Y., Challenges for Rechargeable Li Batteries. *Chemistry of Materials* **2010**, *22* (3), 587-603.
2. Xu, K., Nonaqueous liquid electrolytes for lithium-based rechargeable batteries. *Chem Rev* **2004**, *104* (10), 4303-4417.
3. Jung, Y. S.; Oh, D. Y.; Nam, Y. J.; Park, K. H., Issues and Challenges for Bulk-Type All-Solid-State Rechargeable Lithium Batteries using Sulfide Solid Electrolytes. *Isr J Chem* **2015**, *55* (5), 472-485.
4. Janek, J.; Zeier, W. G., A solid future for battery development. *Nature Energy* **2016**, *1*.
5. Kato, Y.; Hori, S.; Saito, T.; Suzuki, K.; Hirayama, M.; Mitsui, A.; Yonemura, M.; Iba, H.; Kanno, R., High-power all-solid-state batteries using sulfide superionic conductors. *Nature Energy* **2016**, *1* (4).
6. Wang, Y.; Richards, W. D.; Ong, S. P.; Miara, L. J.; Kim, J. C.; Mo, Y.; Ceder, G., Design principles for solid-state lithium superionic conductors. *Nat Mater* **2015**, *14* (10), 1026-31.
7. Manthiram, A.; Yu, X.; Wang, S., Lithium battery chemistries enabled by solid-state electrolytes. *Nature Reviews Materials* **2017**, *2* (4).
8. Yabuuchi, N.; Kubota, K.; Dahbi, M.; Komaba, S., Research Development on Sodium-Ion Batteries. *Chem Rev* **2014**, *114* (23), 11636-11682.
9. Che, H.; Chen, S.; Xie, Y.; Wang, H.; Amine, K.; Liao, X.-Z.; Ma, Z.-F., Electrolyte design strategies and research progress for room-temperature sodium-ion batteries. *Energy Environ. Sci.* **2017**, *10* (5), 1075-1101.
10. Hayashi, A.; Noi, K.; Sakuda, A.; Tatsumisago, M., Superionic glass-ceramic electrolytes for room-temperature rechargeable sodium batteries. *Nat Commun* **2012**, *3*, 856.
11. Tanibata, N.; Noi, K.; Hayashi, A.; Tatsumisago, M., Preparation and characterization of highly sodium ion conducting Na₃PS₄-Na₄SiS₄ solid electrolytes. *RSC Adv.* **2014**, *4* (33), 17120-17123.
12. Zhang, L.; Yang, K.; Mi, J. L.; Lu, L.; Zhao, L. R.; Wang, L. M.; Li, Y. M.; Zeng, H., Na₃PSe₄: A Novel Chalcogenide Solid Electrolyte with High Ionic Conductivity. *Adv Energy Mater* **2015**, *5* (24).
13. Banerjee, A.; Park, K. H.; Heo, J. W.; Nam, Y. J.; Moon, C. K.; Oh, S. M.; Hong, S. T.; Jung, Y. S., Na₃SbS₄: A Solution Processable Sodium Superionic Conductor for All-Solid-State Sodium-Ion Batteries. *Angew Chem Int Edit* **2016**, *55* (33), 9634-9638.
14. Chu, I. H.; Kompella, C. S.; Nguyen, H.; Zhu, Z.; Hy, S.; Deng, Z.; Meng, Y. S.; Ong, S. P.,

- Room-Temperature All-solid-state Rechargeable Sodium-ion Batteries with a Cl-doped Na₃PS₄ Superionic Conductor. *Sci Rep* **2016**, *6*, 33733.
15. Yu, Z.; Shang, S. L.; Seo, J. H.; Wang, D.; Luo, X.; Huang, Q.; Chen, S.; Lu, J.; Li, X.; Liu, Z. K.; Wang, D., Exceptionally High Ionic Conductivity in Na₃P_{0.62}As_{0.38}S₄ with Improved Moisture Stability for Solid-State Sodium-Ion Batteries. *Adv Mater* **2017**, *29* (16).
 16. Jansen, M.; Henseler, U., Synthesis, Structure Determination, and Ionic-Conductivity of Sodium Tetrathiophosphate. *Journal of Solid State Chemistry* **1992**, *99* (1), 110-119.
 17. Hu, Y.-S., Batteries: Getting solid. *Nature Energy* **2016**, *1* (4).
 18. Yang, Z. G.; Zhang, J. L.; Kintner-Meyer, M. C. W.; Lu, X. C.; Choi, D. W.; Lemmon, J. P.; Liu, J., Electrochemical Energy Storage for Green Grid. *Chem Rev* **2011**, *111* (5), 3577-3613.
 19. Park, K. H.; Oh, D. Y.; Choi, Y. E.; Nam, Y. J.; Han, L.; Kim, J.-Y.; Xin, H.; Lin, F.; Oh, S. M.; Jung, Y. S., Solution-Processable Glass LiI-Li₄SnS₄ Superionic Conductors for All-Solid-State Li-Ion Batteries. *Adv. Mater.* **2016**, *28*, 1874-1883.
 20. Tanibata, N.; Noi, K.; Hayashi, A.; Kitamura, N.; Idemoto, Y.; Tatsumisago, M., X-ray Crystal Structure Analysis of Sodium-Ion Conductivity in 94 Na₃PS₄·6 Na₄SiS₄ Glass-Ceramic Electrolytes. *ChemElectroChem* **2014**, *1* (7), 1130-1132.
 21. Zhu, Z.; Chu, I.-H.; Deng, Z.; Ong, S. P., Role of Na⁺ Interstitials and Dopants in Enhancing the Na⁺ Conductivity of the Cubic Na₃PS₄ Superionic Conductor. *Chemistry of Materials* **2015**, *27* (24), 8318-8325.
 22. Rao, R. P.; Chen, H.; Wong, L. L.; Adams, S., Na_{3+x}M_xP_{1-x}S₄ (M = Ge⁴⁺, Ti⁴⁺, Sn⁴⁺) enables high rate all-solid-state Na-ion batteries Na_{2+2δ}Fe_{2-δ}(SO₄)₃|Na_{3+x}M_xP_{1-x}S₄|Na₂Ti₃O₇. *J. Mater. Chem. A* **2017**, *5* (7), 3377-3388.
 23. Wang, H.; Chen, Y.; Hood, Z. D.; Sahu, G.; Pandian, A. S.; Keum, J. K.; An, K.; Liang, C., An Air-Stable Na₃SbS₄ Superionic Conductor Prepared by a Rapid and Economic Synthetic Procedure. *Angew Chem Int Edit* **2016**, *55* (30), 8551-8555.
 24. Bo, S.-H.; Wang, Y.; Kim, J. C.; Richards, W. D.; Ceder, G., Computational and Experimental Investigations of Na-Ion Conduction in Cubic Na₃PSe₄. *Chem. Mater.* **2016**, *28*, 252.
 25. Yu, C.; Ganapathy, S.; de Klerk, N. J. J.; van Eck, E. R. H.; Wagemaker, M., Na-ion dynamics in tetragonal and cubic Na₃PS₄, a Na-ion conductor for solid state Na-ion batteries. *J Mater Chem A* **2016**, *4* (39), 15095-15105.
 26. Park, J. K., *Principles and applications of lithium secondary batteries*. Hong-Rung Publishing Company: **2014**.
 27. T. Nagaura, K. T., Lithium-ion rechargeable battery. *Prog. Batt. Solar Cells* **1990**, *9*, 209-

- 217.
28. Wang, B.; Bates, J. B.; Hart, F. X.; Sales, B. C.; Zuhr, R. A.; Robertson, J. D., Characterization of thin-film rechargeable lithium batteries with lithium cobalt oxide cathodes. *Journal of the Electrochemical Society* **1996**, *143* (10), 3203-3213.
 29. Bates, J. B.; Dudney, N. J.; Neudecker, B.; Ueda, A.; Evans, C. D., Thin-film lithium and lithium-ion batteries. *Solid State Ionics* **2000**, *135* (1-4), 33-45.
 30. Kamaya, N.; Homma, K.; Yamakawa, Y.; Hirayama, M.; Kanno, R.; Yonemura, M.; Kamiyama, T.; Kato, Y.; Hama, S.; Kawamoto, K.; Mitsui, A., A lithium superionic conductor. *Nat Mater* **2011**, *10* (9), 682-6.
 31. Seino, Y.; Ota, T.; Takada, K.; Hayashi, A.; Tatsumisago, M., A sulphide lithium super ion conductor is superior to liquid ion conductors for use in rechargeable batteries. *Energy Environ. Sci.* **2014**, *7* (2), 627-631.
 32. Sakuda, A.; Hayashi, A.; Tatsumisago, M., Sulfide Solid Electrolyte with Favorable Mechanical Property for All-Solid-State Lithium Battery. *Sci Rep-Uk* **2013**, *3*.
 33. Vignarooban, K.; Kushagra, R.; Elango, A.; Badami, P.; Mellander, B. E.; Xu, X.; Tucker, T. G.; Nam, C.; Kannan, A. M., Current trends and future challenges of electrolytes for sodium-ion batteries. *Int J Hydrogen Energ* **2016**, *41* (4), 2829-2846.
 34. Zhang, J. W.; Huang, X. B.; Wei, H.; Fu, J. W.; Huang, Y. W.; Tang, X. Z., Enhanced electrochemical properties of polyethylene oxide-based composite solid polymer electrolytes with porous inorganic-organic hybrid polyphosphazene nanotubes as fillers. *J Solid State Electr* **2012**, *16* (1), 101-107.
 35. Cao, C. Y.; Wang, H. B.; Liu, W. W.; Liao, X. Z.; Li, L., Nafion membranes as electrolyte and separator for sodium-ion battery. *Int J Hydrogen Energ* **2014**, *39* (28), 16110-16115.
 36. Palomares, V.; Serras, P.; Villaluenga, I.; Hueso, K. B.; Carretero-Gonzalez, J.; Rojo, T., Na-ion batteries, recent advances and present challenges to become low cost energy storage systems. *Energy & Environmental Science* **2012**, *5* (3), 5884-5901.
 37. Wenzel, S.; Leichtweiss, T.; Weber, D. A.; Sann, J.; Zeier, W. G.; Janek, J., Interfacial Reactivity Benchmarking of the Sodium Ion Conductors Na₃PS₄ and Sodium beta-Alumina for Protected Sodium Metal Anodes and Sodium All-Solid-State Batteries. *ACS Appl Mater Interfaces* **2016**.
 38. Guin, M.; Tietz, F., Survey of the transport properties of sodium superionic conductor materials for use in sodium batteries. *Journal of Power Sources* **2015**, *273*, 1056-1064.
 39. Guin, M.; Tietz, F.; Guillon, O., New promising NASICON material as solid electrolyte for sodium-ion batteries: Correlation between composition, crystal structure and ionic conductivity of Na_{3+x}Sc₂Si_xP_{3-x}O₁₂. *Solid State Ionics* **2016**, *293*, 18-26.

40. Kotobuki, M.; Munakata, H.; Kanamura, K.; Sato, Y.; Yoshida, T., Compatibility of $\text{Li}_7\text{La}_3\text{Zr}_2\text{O}_{12}$ Solid Electrolyte to All-Solid-State Battery Using Li Metal Anode. *Journal of the Electrochemical Society* **2010**, *157* (10), A1076-A1079.
41. Kim, K. H.; Iriyama, Y.; Yamamoto, K.; Kumazaki, S.; Asaka, T.; Tanabe, K.; Fisher, C. A. J.; Hirayama, T.; Murugan, R.; Ogumi, Z., Characterization of the interface between LiCoO_2 and $\text{Li}_7\text{La}_3\text{Zr}_2\text{O}_{12}$ in an all-solid-state rechargeable lithium battery. *Journal of Power Sources* **2011**, *196* (2), 764-767.
42. Bruce, P. G., *Solid state electrochemistry*. Cambridge University: **1995**.
43. Hendrick, Jr; Bray, P. J., Phenomenological equation for NMR motional narrowing in solids. *J. Magn. Reson.* **1973**, *9* (3), 341-357.
44. He, X.; Zhu, Y.; Mo, Y., Origin of fast ion diffusion in super-ionic conductors. *Nat. Commun.* **2017**, *8*, 15893.
45. Wei, S. H.; Zhang, S. B., Chemical trends of defect formation and doping limit in II-VI semiconductors: The case of CdTe. *Phys Rev B* **2002**, *66* (15).
46. Richards, W. D.; Tsujimura, T.; Miara, L. J.; Wang, Y.; Kim, J. C.; Ong, S. P.; Uechi, I.; Suzuki, N.; Ceder, G., Design and synthesis of the superionic conductor $\text{Na}_{10}\text{SnP}_2\text{S}_{12}$. *Nat Commun* **2016**, *7*, 11009.